# 32 Scanning Probe Microscopy on Polymer Solar Cells

*Joachim Loos · Alexander Alexeev*

**Abstract.** Polymer solar cells have the potential to become a major electrical power generating tool in the twenty-first century. Research and development endeavors are focusing on continuous roll-to-roll printing of polymeric or organic compounds from solution—like newspapers—to produce flexible and lightweight devices at low cost. It is recognized, though, that besides the functional properties of the compounds, the organization of structures on the nanometre level—forced and controlled mainly by the processing conditions applied—determines the performance of state-of-the-art polymer solar cells. In such devices the photoactive layer is composed of at least two functional materials that form nanoscale interpenetrating phases with specific functionalities, a so-called bulk heterojunction. In this study, we discuss our current knowledge of the main factors determining the morphology formation and evolution—based on systematic scanning probe microscopy studies—and gaps in our understanding of nanoscale structure–property relations in the field of high-performance polymer solar cells are addressed.

**Key words:** Polymer solar cells, AFM, Conductive AFM, SNOM, Morphology, Nanoscale functional properties

## Abbreviations

| | |
|---|---|
| AFM | Atomic force microscopy |
| C-AFM | Conductive atomic force microscopy |
| EFTEM | Energy-filtered transmission electron microscopy |
| HOMO | Highest occupied molecular orbital |
| ITO | Indium tin oxide |
| LUMO | Lowest unoccupied molecular orbital |
| MEH-PPV | Poly[2-methoxy-5-(2′-ethylhexyloxy)-1,4-phenylene vinylene] |
| MDMO-PPV | Poly[2-methoxy-5-(3′,7′-dimethyloctyloxy)-1,4-phenylene vinylene] |
| P3HT | Poly(3-hexylthiophene) |
| PCBM | [6,6]-Phenyl $C_{61}$ butyric acid methyl ester |
| PCNEPV | Poly[oxa-1,4-phenylene-(1-cyano-1,2-vinylene)-(2-methoxy-5-(3,7-dimethyloctyloxy)-1,4-phenylene)-1,2-(2-cyanovinylene)-1,4-phenylene] |
| PEDOT-PSS | Poly(ethylenedioxythiophene)–poly(styrene sulfonate) |
| PSC | Polymer solar cell |
| rms | Root mean square |
| SNOM | Scanning near-field optical microscopy |
| SPM | Scanning probe microscopy |
| STM | Scanning tunnelling microscopy |
| TEM | Transmission electron microscopy |

## 32.1 Brief Introduction to Polymer Solar Cells

Organic electronics has the potential to become one of the major industries of the twenty-first century. Research and development endeavours are focusing on continuous roll-to-roll printing of polymeric or organic compounds from solution—like newspapers—to produce flexible and lightweight devices at low cost. In particular, polymeric semiconductor-based solar cells are currently in investigation as potential low-cost devices for sustainable solar energy conversion. Because they are large-area electronic devices, readily processed polymeric semiconductors from solution have an enormous cost advantage over inorganic semiconductors. Further benefits are the low weight and flexibility of the resulting thin-film devices (Fig. 32.1). Despite the progress made in the field, it is clear that polymer solar cells (PSCs) are still in their early research and development stage. Several issues must be addressed before PSCs will become practical devices. These includes further understanding of operation and stability of these cells, and the control of the morphology formation—mainly the morphology of the active layer—which is directly linked to the performance of devices.

Figure 32.2 shows the characteristic architecture of a device. It is constructed of an indium tin oxide (ITO) back electrode deposed on glass, a poly(ethylenedioxythiophene)–poly(styrene sulfonate) (PEDOT-PSS) layer, the photoactive layer composed—in the present case—of the $C_{60}$-derivatized methanofullerene [6,6]-phenyl $C_{61}$ butyric acid methyl ester (PCBM) blended with poly[2-methoxy-5-(3′,7′-dimethyloctyloxy)-1,4-phenylene vinylene] (MDMO-PPV), and the top aluminium electrode. During processing of the device, the surface topography of each individual layer was measured. Both the PEDOT-PSS and the MDMO-PPV/PCBM layers are rather smooth, while the ITO and the thermally evaporated Al have a large roughness.

One of the main differences between inorganic and organic semiconductors is the magnitude of the exciton binding energy (an exciton is a bound electron–hole pair). In many inorganic semiconductors, the binding energy is small compared to the thermal energy at room temperature and therefore free charges are created under ambient conditions upon excitation across the band gap [2]. An organic semiconductor, on the other hand, typically possesses an exciton binding energy that exceeds $kT$

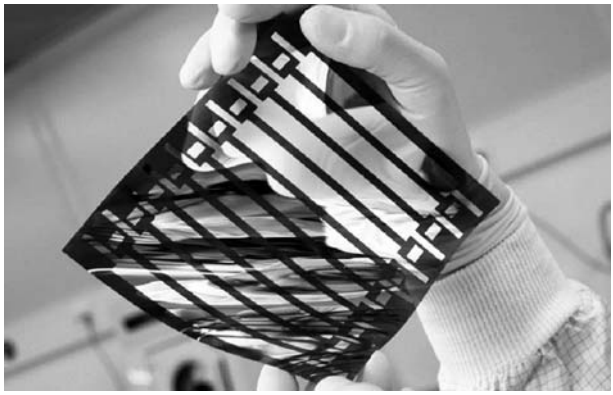

**Fig. 32.1.** Large-area, flexible and printable polymer solar cell demonstrated by Siemens, Germany

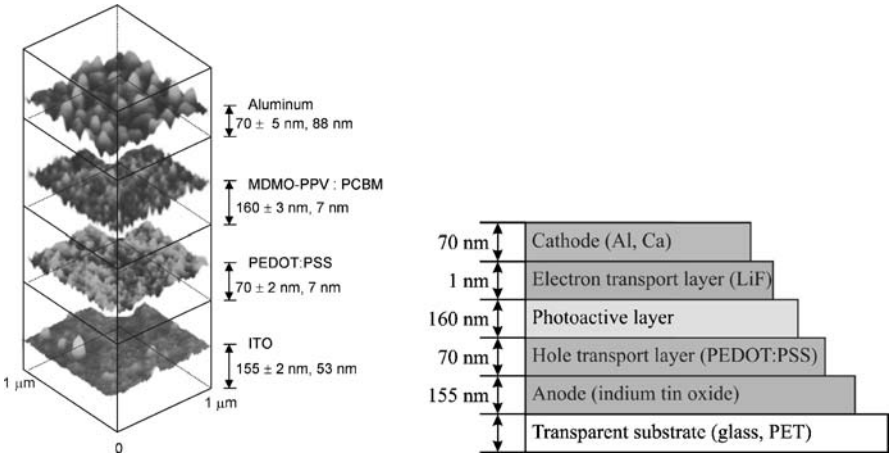


**Fig. 32.2.** *Left*: Atomic force microscopy (AFM) images of the surface of the different layers of a glass/ITO/PEDOT-PSS/MDMO-PPV/PCBM (1:4 wt%)/Al polymer solar cell. For each layer the thickness as determined by a surface profiler, the root mean square roughness of $1 \times 1\ \mu m^2$ area, and the peak-to-peak variations as determined by AFM are indicated. *Right*: A polymer solar cell. *ITO* indium tin oxide, *PEDOT* poly(ethylenedioxythiophene), *PSS* poly(styrene sulfonate), *MDMO-PPV* poly[2-methoxy-5-(3′,7′-dimethyloctyloxy)-1,4-phenylene vinylene], *PCBM* [6,6]-phenyl $C_{61}$ butyric acid methyl ester, *PET* poly(ethylene terephthalate). (Reprinted with permission from [1]. Copyright 2002 Wiley-VCH)

(roughly by more than an order of magnitude) [3]. As a consequence, excitons are formed upon excitation instead of free charges. This difference between inorganic and organic semiconductors is of critical importance in PSCs. While in conventional, inorganic solar cells, free charges are created upon light absorption, PSCs need an additional mechanism to dissociate the excitons.

A successful method to dissociate bound electron–hole pairs in organic semiconductors is the so-called donor/acceptor interface. This interface is formed between two organic semiconductors with different valence and conduction bands, or equivalently dissimilar highest occupied molecular orbital (HOMO) and lowest unoccupied molecular orbital (LUMO) levels, respectively. The donor material is the material with the lowest ionization potential, and the acceptor material the one with the largest electron affinity. If an exciton is created in the photoactive layer and reaches the donor/acceptor interface, the electron will be transferred to the acceptor material and the hole will recede in the donor material. Afterwards, both charge carriers move to their respective electrode when electrode materials are chosen with the right work functions.

Considerable photovoltaic effects of organic semiconductors applying the heterojunction approach were demonstrated first by Tang [4] in the 1980s. A thin-film, two-layer organic photovoltaic cell has been fabricated that showed a power conversion efficiency of about 1% and large fill factor, which is the ratio of the maximum power ($V_{mp}J_{mp}$) divided by the short-circuit current ($I_{sc}$) and the open-circuit voltage ($V_{oc}$) in the light current density–voltage ($I$–$V$) characteristics, of 0.65 under simulated AM2 illumination (two suns equivalent).

The external quantum efficiency $\eta_{EQE}$ of a photovoltaic cell based on exciton dissociation at a donor/acceptor interface is $\eta_{EQE} = \eta_A \eta_{ED} \eta_{CC}$ [5], with the light absorption efficiency $\eta_A$, the exciton diffusion efficiency $\eta_{ED}$, which is the fraction of photogenerated excitons that reaches a donor/acceptor interface before recombining, and the carrier collection efficiency $\eta_{CC}$, which is the probability that a free carrier that is generated at a donor/acceptor interface by dissociation of an exciton reaches its corresponding electrode. Donor/acceptor interfaces can be very efficient in separating excitons: systems are known in which the forward reaction, the charge-generation process, takes place on the femtosecond time scale, while the reverse reaction, the charge-recombination step, occurs in the microsecond range [6]. The typical exciton diffusion length in organic semiconductors, and in particular in conjugated polymers, however, is limited to approximately 10 nm [7–9]. These characteristics result in the limitation of the efficiency of such solar cells based on the approach of thin-film bilayer donor/acceptor interface: for maximum light absorption the active layer should be thick, at least hundreds of nanometres; in contrast, for charge generation the interface between donor and acceptor should be maximized and located near the place where the excitons are formed. Both requirements cannot be fulfilled at the same time by bilayer heterojunctions.

Independently, Yu et al. and Halls et al. have addressed the problem of limited exciton diffusion length by intermixing two conjugated polymers with different electron affinities [11, 12], or a conjugated polymer with $C_{60}$ molecules or their methanofullerene derivatives [13]. Because phase separation occurs between the two components, a large internal interface is created so that most excitons would be formed near the interface, and can be dissociated at the interface. In case of the polymer/polymer intermixed film, evidence for the success of the approach has been found in the observation that the photoluminescence from each of the polymers was quenched. This implies that the excitons generated in one polymer within the intermixed film reach the interface with the other polymer and dissociate before recombining. This device structure, a so-called bulk heterojunction (Fig. 32.3), provides a route by which nearly all photogenerated excitons in the film can be split into free charges. At present bulk heterojunction structures are the main candidates for high-efficiency PSCs. Tailoring their morphology towards optimized performance is a challenge, though.

Several requirements for the photoactive layer of a PSC can be summarized (Table 32.1). Firstly, since the range of the absorption spectrum of the currently used donor materials is insufficient for optimum utilization of the incident light, photoinduced absorption of the cell should better fit the solar spectrum, which requires, e. g., lower band gap polymers to capture more near-IR photons. To enhance absorption capability, the photoactive layer should be thick enough to absorb more photons from incident light, which needs layers with a thickness of hundreds of nanometres. To achieve a bulk-heterojunction structure in the photoactive layer with appropriate thickness via solvent-based thin film deposition technology, a high solubility or well dispersivity of all the constituents in the solvent is a prerequisite. During solidification of the constituents from the solution and thus formation of a thin film, a few methods could be used to tune the morphology of the thin blend film towards the optimum bulk heterojunction, applying both thermodynamic and kinetic aspects. The Flory–Huggins parameter $\chi$ between the compounds describes

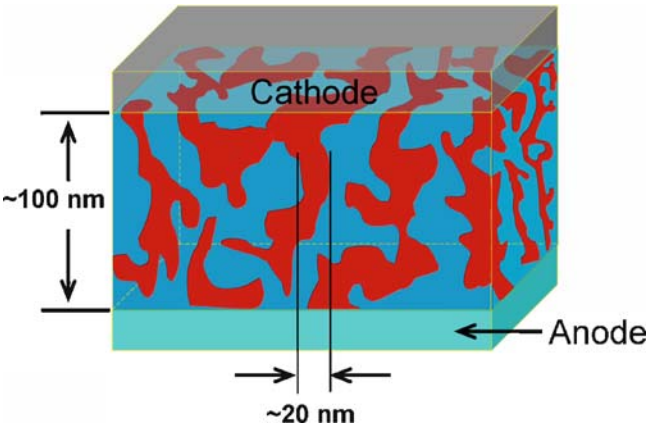


**Fig. 32.3.** Three-dimensional representation of a bulk heterojunction (electron donor and acceptor compounds in *different colours*) with top and back electrodes. (Reprinted with permission from [10]. Copyright 2007 American Chemical Society)

**Table 32.1.** Molecular and morphology requirements for the photoactive layer of a high-performance polymer solar cell

| Requirement | Influenced by molecular architecture | Morphology |
|---|---|---|
| Utilization of incident light | Molecule design to tune band gap(s) | Layer thickness, roughness of interfaces |
| Exciton dissociation | Match of band properties between donor and acceptor | Maximum interface<br>Small acceptor/donor phases within exciton diffusion range |
| Charge transport | Molecule design with high charge carrier mobility | Short and continuous pathways to the electrodes<br>Ordered (crystalline) transportation pathways |

the main driving force for phase segregation in a blend from the thermodynamics point of view, in which the ratio between the compounds and the conformation of the conjugated polymers in the solution are the key aspects to determine the length scale of phase separation. The kinetic issues also have a significant influence on the morphology of the thin blend film eventually obtained. For instance, by applying spin-coating, one obtains a thin blend film with rather homogeneous morphology; for preparation methods like film-casting, on the other hand, the same blend usually undergoes large-scale phase separation and a more equilibrium organization is achieved during film formation [14]. Therefore, both thermodynamic aspects as well as kinetics determine the organization of the bulk-heterojunction photoactive layer in PSCs, i.e. by controlled tuning of the formation process of the active layer, one can form a nanoscale interpenetrating network with, probably, crystalline order of

both constituents [15,16]. Further, an appropriate length scale of phase separation in the photoactive layer is the key point for high-performing PSCs. To realize this "appropriate" length scale of phase separation, one has to make a compromise between the interface area and efficient pathways for the transportation of free charge carriers towards correct electrodes so as to reduce charge carrier recombination within the photoactive layer.

In the following sections we introduce preparation approaches and routes towards creating the desired morphology of the photoactive layer of a PSC. In particular, we discuss in detail the influence of the constituents and solvent used, composition, and annealing treatments on morphology formation. Moreover, we highlight the importance of scanning probe microscopy (SPM) techniques to provide the required information on the local nanometre-scale organization of the active layer as well as its local functional properties such as optical absorbance and conductivity.

## 32.2 Sample Preparation and Characterization Techniques

Various blends based on the following compounds have been used as active layers for PSCs: blends of MDMO-PPV [17] as an electron donor and the $C_{60}$ derivative PCBM [18] or poly[oxa-1,4-phenylene-(1-cyano-1,2-vinylene)-(2-methoxy-5-(3,7-dimethyloctyloxy)-1,4-phenylene)-1,2-(2-cyanovinylene)-1,4-phenylene] (PCNEPV) as an electron acceptor. Further, blends of poly(3-hexylthiophene) (P3HT) with PCBM have been investigated. The average molecular masses of the MDMO-PPV, PCNEPV and P3HT used were 570, 113.5 and 100 kg/mol, respectively, as determined by gel permeation chromatography using polystyrene standards. The chemical structures of the polymers are presented in Fig. 32.4. PEDOT-PSS was purchased from Bayer, Germany.

For preparation of the active layer the compounds were dissolved in suitable solvents (e. g. 1,2-dichlorobenzene) and deposited by spin-coating on glass substrates covered with about 100-nm-thick thick layers of ITO and PEDOT-PSS that form the electrode for hole collection. Spin-coating conditions were adjusted such that a film thickness of the active layer of about 50–200 nm could be established. Such samples represent working photovoltaic devices, except for the missing metal back electrode. For conventional device characterization, an Al top electrode was used.

Thermal annealing was performed on complete devices, i. e. with the photoactive layer between electrodes, or on structures without a top electrode at various temperatures and times; annealing experiments were conducted in situ and ex situ, i. e. at corresponding annealing temperature or after annealing and cooling down to room temperature. More details on the compounds used as well as on layer or device preparation can be found in [19,20].

SPM measurements were performed with the commercial microscopes Solver P47H, Solver LS and NTEGRA Aura (all NT-MDT, Moscow, Russia) equipped with optical microscopes. The cantilevers used were CSC12 (Micromash) and NSG11 (NT-MDT), and conductive tips of both types were used with an additional Au coating. Height measurements were calibrated using a 25-nm-height standard grating produced by NT-MDT. The typical force constant of the cantilever used for electrical

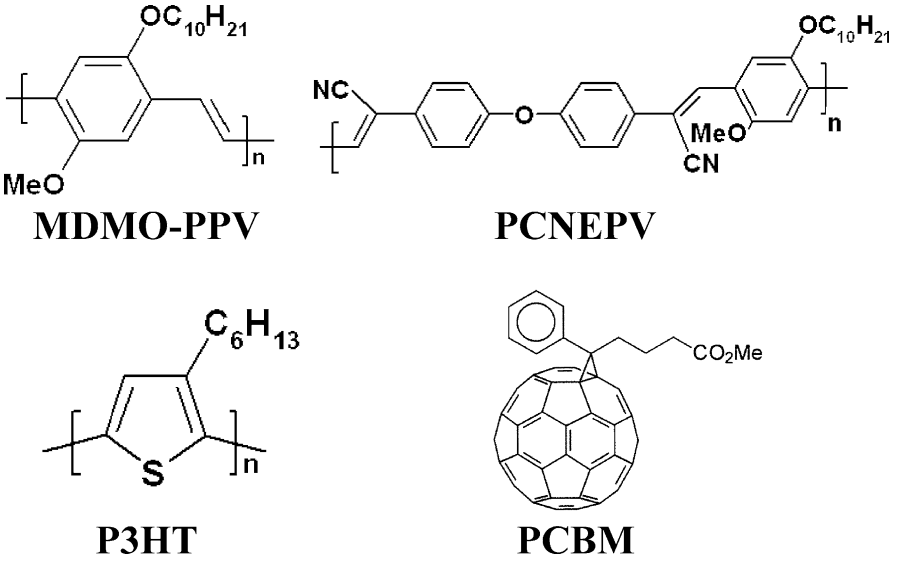


**Fig. 32.4.** Some suitable conjugated polymers and the fullerene derivative PCBM applied in polymer solar cells. *PCNEPV* poly[oxa-1,4-phenylene-(1-cyano-1,2-vinylene)-(2-methoxy-5-(3,7-dimethyloctyloxy)-1,4-phenylene)-1,2-(2-cyanovinylene)-1,4-phenylene], *P3HT* poly(3-hexylthiophene)

measurements was about 0.65 N/m, and the radius was below 50 nm. For annealing experiments, the Solver P47H instrument was operated in intermittent-contact mode under ambient conditions, and its integrated high-temperature heating stage was employed to acquire the abovementioned in situ and ex situ data. The temperature stability of the hot stage was controlled to within 0.1 °C.

Since the polymers are sensitive to oxygen, some atomic force microscopy (AFM) measurements were performed in a glove box (Unilab, M. Braun) having a nitrogen atmosphere with oxygen and water levels below 1 ppm. For conductive AFM (C-AFM) characterization the ITO layer was grounded during all SPM measurements. Current–voltage ($I$–$V$) characteristics were measured with and without illumination. The Fermi levels for ITO, PEDOT-PSS and gold, respectively, are 4.7, 5.2 and 5.1 eV [21, 22]. For reason of better illustration, Fig. 32.5 shows a scheme of the experimental setup for C-AFM measurements.

For scanning near-field optical microscopy (SNOM) measurements, the active layers of PSCs were transferred to glass slides. Measurements were performed using Nanofinder and NTEGRA Spectra instruments (NT-MDT, Moscow, Russia, and Tokyo Instruments, Japan). The scanning near-field optical microscope head with a single-mode optical fibre coated with aluminium was operated in transmission mode. The probes with a tip aperture of 100 nm were prepared by chemical etching and have a transmission efficiency of $10^{-3}$–$10^{-4}$ and maximum output power of 5 μW. Two lasers, He–Ne ($\lambda = 632.8$ nm) and Nd–YAG ($\lambda = 532$ nm) were employed as radiation sources. The transmitted light was collected with a ×20 objective and detected with a photomultiplier tube. For each line scan 256 data points were taken with a line scan frequency of 0.8–1.0 Hz.

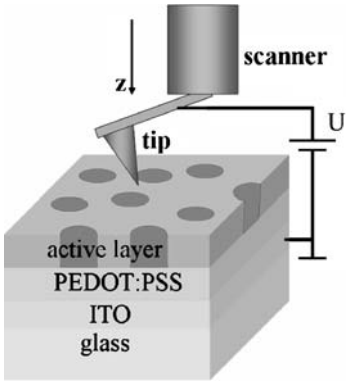


**Fig. 32.5.** The sample structure with segregated phases and the conductive AFM experimental setup, including a scanner and a conductive tip

## 32.3 Morphology Features of the Photoactive Layer

### 32.3.1 Influence of Composition and Solvents on the Morphology of the Active Layer

Intensive morphology studies have been performed on polymer/methanofullerene systems, in which the $C_{60}$ derivative PCBM was applied [18, 23]. So far PCBM is the most widely used electron acceptor and the most successful PSCs are obtained by mixing it with the donor polymers MDMO-PPV and other PPV derivatives [24, 25], or with P3HT [26–30]. PCBM has an electron mobility of $2 \times 10^{-3}$ cm$^2$/V/s [31], and compared with $C_{60}$, the solubility of PCBM in organic solvents is greatly improved, which allows the utilization of film-deposition techniques requiring highly concentrated solutions. After applying chlorobenzene as a solvent Shaheen et al. [24] found a dramatic increase in power conversion efficiency of spin-cast MDMO-PPV/PCBM to 2.5%, whereas for the same preparation conditions but using toluene as the solvent only 0.9% power conversion efficiency was obtained. Recently, a more comprehensive study on the influence of solvents on morphology formation was performed by Rispens et al. [32]. They compared the surface topography of MDMO-PPV/PCBM active layers by varying the solvent from xylene through chlorobenzene to 1,2-dichlorobenzene and found a decrease in phase separation from xylene through chlorobenzene to 1,2-dichlorobenzene (Fig. 32.6).

Besides the solvent used and the evaporation rate applied, the overall compound concentration and the ratio between the two compounds in the solution are important parameters controlling morphology formation; e. g. high compound concentrations induce large-scale phase segregation upon film formation [33]. For the systems MDMO-PPV/PCBM and poly[2-methoxy-5-(2′-ethylhexyloxy)-1,4-phenylene vinylene] (MEH-PPV)/PCBM the optimum ratio of the compounds is about 1:4. Initial studies with $C_{60}$ show that the photoluminescence of PPV could be quenched for much lower $C_{60}$ concentrations [9]. It has been demonstrated that with increasing PCBM concentration the cluster size increases accordingly [14, 34]. Recently van Duren et al. [19] introduced a comprehensive study relating the morphology of MDMO-PPV/PCBM blends to solar cell performance. The amounts of

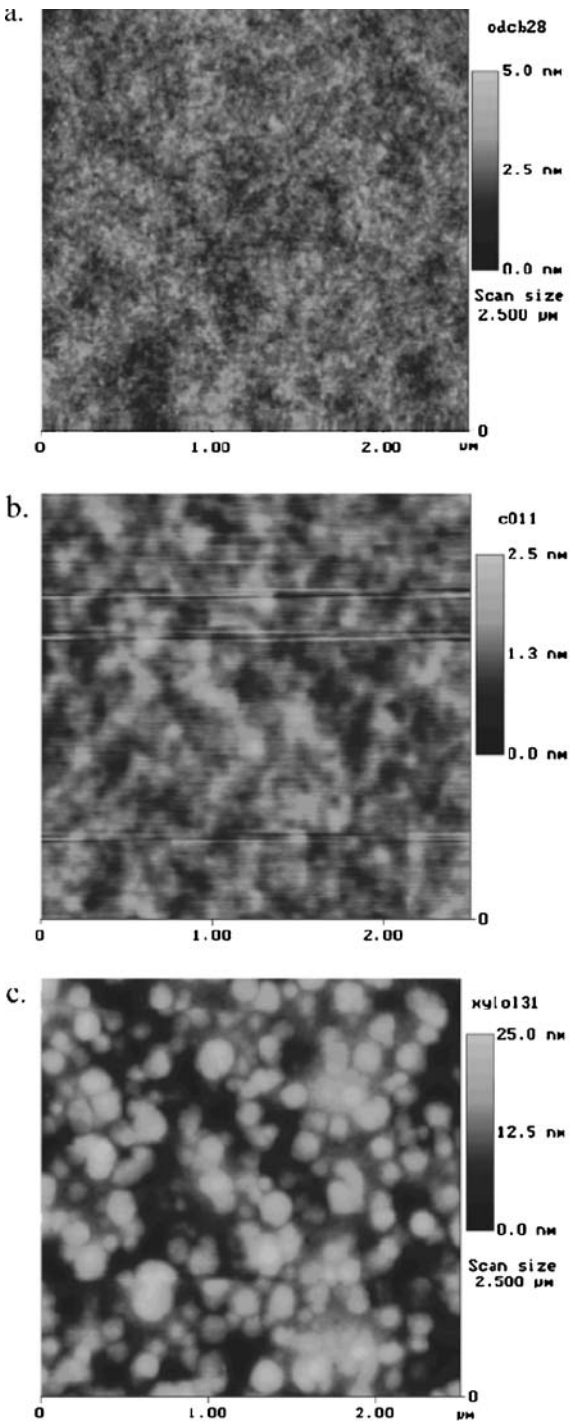


**Fig. 32.6.** Surface of MDMO-PPV/PCBM (1:4 weight ratio) composites, spin-cast from 0.4 polymer wt% solutions. **a** 1,2-Dichlorobenzene; **b** chlorobenzene; **c** xylene. (Reprinted with permission from [32]. Copyright 2003 Royal Society of Chemistry)

MDMO-PPV and PCBM spanned a wide range. Figure 32.7 shows the height and corresponding phase contrast images obtained by AFM for blend films for four different compositions. Apart from the compositions for the images shown in Fig. 32.7 compositions of 0, 33, 50, 67, 75, 80, 90 and 100 wt% PCBM in MDMO-PPV have been studied. The height images reveal extremely smooth surfaces for the pure compounds and blends with PCBM concentrations of 2–50 wt% with a peak-to-valley roughness of about 3 nm and root-mean-square (rms) values of 0.4 nm for an investigated area of 2 μm × 2 μm. The surface becomes increasingly rough for 67–90 wt% PCBM, with a peak-to-valley roughness of about 3–22 nm and rms values of 0.4–3.3 for the same investigated area size of 2 μm × 2 μm, and a reproducible phase contrast appears. Separate domains of one phase in a matrix of another phase can easily be recognized at these higher concentrations of PCBM. The domain size increases from 45–65 nm for 67 wt% PCBM to 110–200 nm for 90 wt% PCBM. For 80 wt% PCBM blend films, a gradual but small increase in domain size from 60–80 to 100–130 nm was observed when the film thickness was increased in steps from 65 to 270 nm. In summary, for PCBM contents less than 50 wt%, rather homogeneous

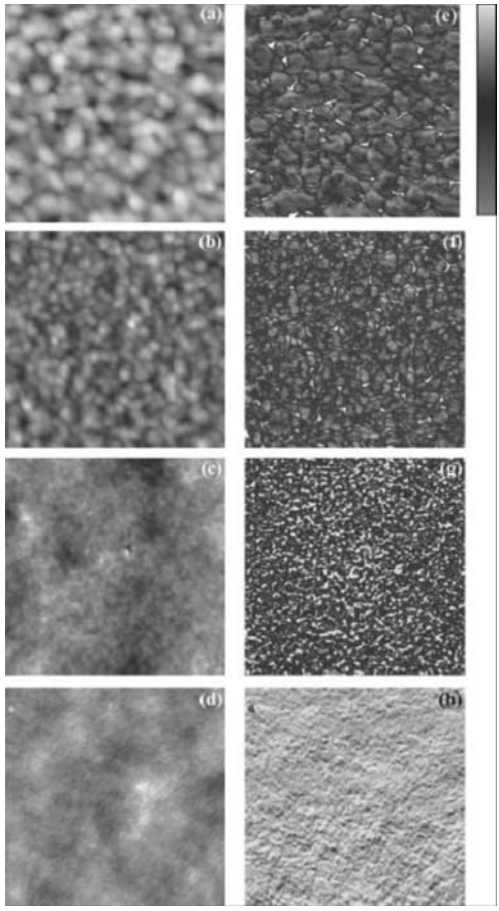


**Fig. 32.7.** The AFM height (**a**–**d**) and simultaneously taken phase (**e**–**h**) images of the MDMO-PPV/PCBM films of 90 wt % (**a**, **e**), 80 wt % (**b**, **f**), 67 wt % (**c**, **g**), and 50 wt % (**d**, **h**) PCBM. The *height bar* (maximum peak-to-valley) represents 20 nm (**a**), 10 nm (**b**) and 3 nm (**c**, **d**). The size of the images is 2 × 2 $\mu m^2$. (Reprinted with permission from [19]. Copyright 2004 Wiley-VCH)

film morphology is observed, and for 50 wt% or more photoluminescence is already quenched, indicating complete exciton dissociation. For concentrations around 67 wt% and higher a rather abrupt improvement in the device properties is found with the observed onset of phase separation. Thus, in general it is concluded that charge transportation rather than charge separation is the limiting factor determining the performance of the corresponding device. Only above the critical concentration of about 67 wt% PCBM forms a nanoscale percolating network within the PPV matrix.

### 32.3.2 Influence of Annealing

Another method to influence the morphology of the active layer of PSCs is application of a controlled thermal posttreatment. The purpose of such treatment is to probe, on the one hand, the long-term stability of the morphology. Improvement of the long-term stability of PSCs in an ambient atmosphere is currently still a challenge. However, an acceptable lifetime is a key point for PSCs to compete with traditional photovoltaic technology and is a prerequisite for commercialization.

In general, the stability of PSCs is limited by two factors. One is the degradation of materials, in particular the conjugated polymers, upon being exposed to oxygen, water or UV radiation. The other limitation comes from the possible morphology instability of the photoactive layer during operation of devices at high temperature (exposed to sunlight, which means at least 60–80 °C is possible!). For the system MDMO-PPV/PCBM annealing always results in large-scale phase separation and dominant formation of large PCBM single crystals, even for short times or low annealing temperatures below the glass-transition temperature of MDMO-PPV of about 80 °C [14, 35], which ultimately corresponds to a significant drop of the efficiency of the corresponding solar cells.

In order to get three-dimensional information of the morphology evolution of the thin blend film on the substrate, and in particular on the PCBM diffusion behaviour, AFM performed in intermittent-contact mode is used to acquire topography images during an annealing process [36]. Figure 32.8 shows a series of AFM topography images of MDMO-PPV/PCBM films recorded in situ upon annealing at 130 °C for different times. For the pristine film before any thermal treatment (as shown in Fig. 32.8a), a homogeneous morphology within a relatively large area is observed at the scanning resolution we used. Actually, the fresh film is composed of PCBM-rich domains with an average size of 80 nm distributed in the relatively PCBM-poor MDMO-PPV/PCBM matrix. For the whole film, PCBM is condensed as nanocrystals adopting various crystallographic orientations as known from corresponding transmission electron microscopy (TEM) studies [14, 37].

Upon annealing, PCBM single crystals grow gradually with annealing time and stick out of the film plane (as shown in Fig. 32.8b–f). Notably, in these AFM topography images, the bright domains are PCBM single crystals (marked as A in Fig. 32.8d); and the dark areas (depletion zones, marked as B in Fig. 32.8d) initially surrounding the PCBM crystals reflect thinner regions of the film, being composed of almost pure MDMO-PPV (i. e. depleted of PCBM). To clearly monitor the evolution of both the PCBM crystals and the depletion zones with time during annealing, a set of cross-sectional profiles across a PCBM single crystal and the surrounding

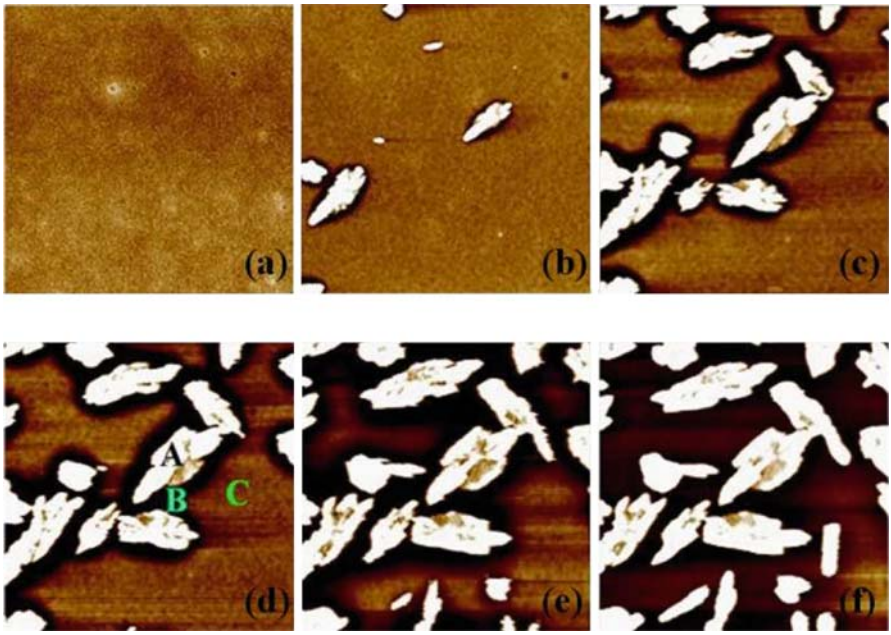


**Fig. 32.8.** AFM topography images of MDMO-PPV/PCBM blend films (MDMO-PPV:PCBM 1:4 by weight) recorded in situ upon annealing at 130 °C for **a** pristine film, **b** 12 min, **c** 22 min, **d** 27 min;,**e** 38 min and **f** 73 min. Scan size 15 × 15 $\mu m^2$; height range (from peak to valley) 200 nm. *A*, *B* and *C* in **d** represent the region where the PCBM nucleates and the crystal grows (*A*), the depletion zone that is formed owing to moving out of PCBM material towards the growing crystal (*B*), and the initial blend film still consisting of both MDMO-PPV and PCBM (*C*), respectively. (Reprinted with permission from [36]. Copyright 2004 American Chemical Society)

depletion zone are shown in Fig. 32.9. After a PCBM single crystal sticks out from the film, the growth continues in both lateral and perpendicular directions. The depletion zone around it becomes broader and deeper as annealing goes on. However, by simply comparing these topography images, we are not able to judge whether there is a difference in growth kinetics between the PCBM crystals and the depletion zones around them, which reflects how the PCBM molecules diffuse within the composite film and finally contribute to the formation of PCBM single crystals. In order to acquire exact growth kinetics for both the PCBM crystals and the depletion zones, volume quantification calculations were applied to topographic images from the composite film annealed for different times similar to the areas shown in Fig. 32.8. but this time the scan size was 100 μm × 100 μm so that detailed volume evolution of either the PCBM single crystals or the depletion zones could be resolved. Since the calculations were carried out based on quite large areas of the composite films, the results make statistical sense.

In an AFM topography image, the main information that each pixel actually carries is a relative height value. For an image with dimensions of 512 × 512 pixels, correspondingly, there are 262 144 height values with the image. If a specific

resolution of the height value is given, a plot can be created which visualizes the total number of pixels that have a specific height value within the given resolution versus the height value. This plot actually gives a height distribution histogram for the whole topography image. As an example, Fig. 32.10 shows the histogram of height counts from the image of Fig. 32.8d. Three dominant peaks can be resolved from this histogram by using Gaussian distribution fitting with good fitting quality of $R^2 = 0.9847$.

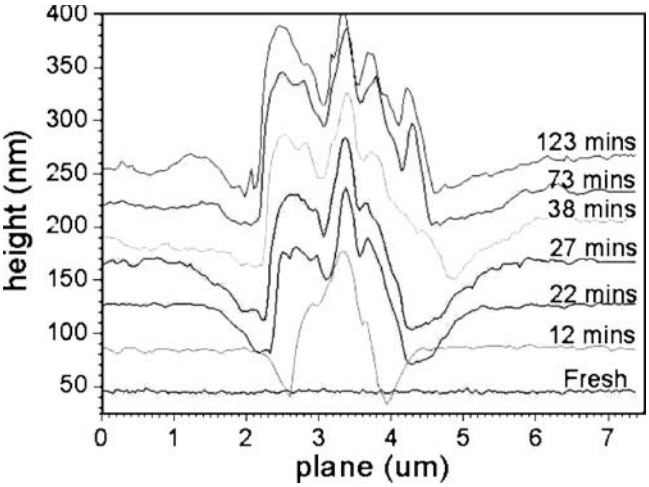


**Fig. 32.9.** Cross-sectional profiles across a PCBM single-crystal cluster and the depletion zone around it recorded in situ during annealing at 130 °C for the given times. The curves have been shifted along the $Y$-axis to give a clearer demonstration. (The sketch is similar to Fig. 2 in [36])

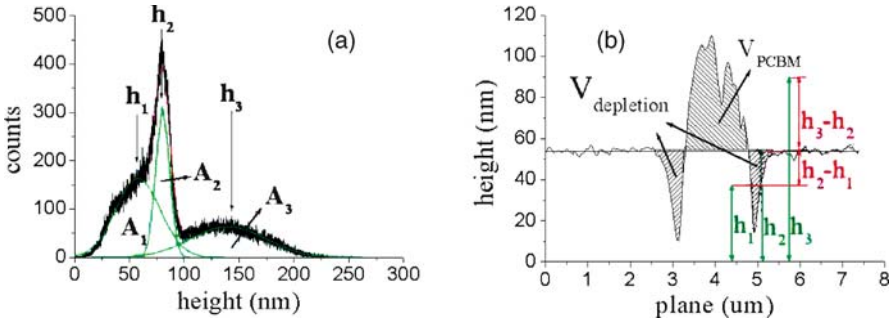


**Fig. 32.10. a** Height distribution histogram obtained from the AFM topography image shown in Fig. 32.8d, which is resolved into three parts $A_1$, $A_2$ and $A_3$. $A_1$ denotes the area of the PCBM single crystals, $A_2$ the area of the depletion zones surrounding the PCBM crystals and $A_3$ the area of the original film plane. $h_1$, $h_2$ and $h_3$ represent the peak positions of Gaussian-fitted curves corresponding to the PCBM single crystals, the depletion zones and the original film plane, respectively. **b** Cross-sectional profile across a PCBM crystal and the depletion zone around it. The values of $h_1$, $h_2$ and $h_3$ were obtained from **a**. (The sketches are similar to Fig. 3 in [36])

As shown in Fig. 32.10a, in a typical height-distribution histogram obtained from a topography image the three Gaussian distribution fitted curves can be assigned to the PCBM single crystals ($A_1$), depletion zones surrounding the PCBM crystals ($A_2$) and the original film surface ($A_3$), respectively. During the posttreatment of each topography image, the smallest height value measured within the whole film is set to zero and the height values of the other pixels are recalculated with respect to this reference to produce a relative height value for each pixel measured. Therefore, as shown in the cross-sectional profile of Fig. 32.10b, $h_1$, $h_2$, and $h_3$, the height values associated with the three peaks corresponding to regions A, B and C as shown in Fig. 32.8d, represent the relative average height of the depletion zones, of the original film surface plane and of the PCBM crystals, respectively. Hence, $h_1 - h_3$ denotes the average height of the PCBM crystals and $h_3 - h_2$ the average depth of the depletion zones with respect to the original film surface plane.

At the initial annealing time, as shown in Fig. 32.11a, the volume of the film collapsed in the depletion area is smaller compared with that of the diffused PCBM inserted in the crystals. As annealing goes on, more and more PCBM diffuses towards the crystals, which ultimately causes a sudden collapse of large areas of the remaining MDMO-PPV matrix, which contributes to the rapid increase in the

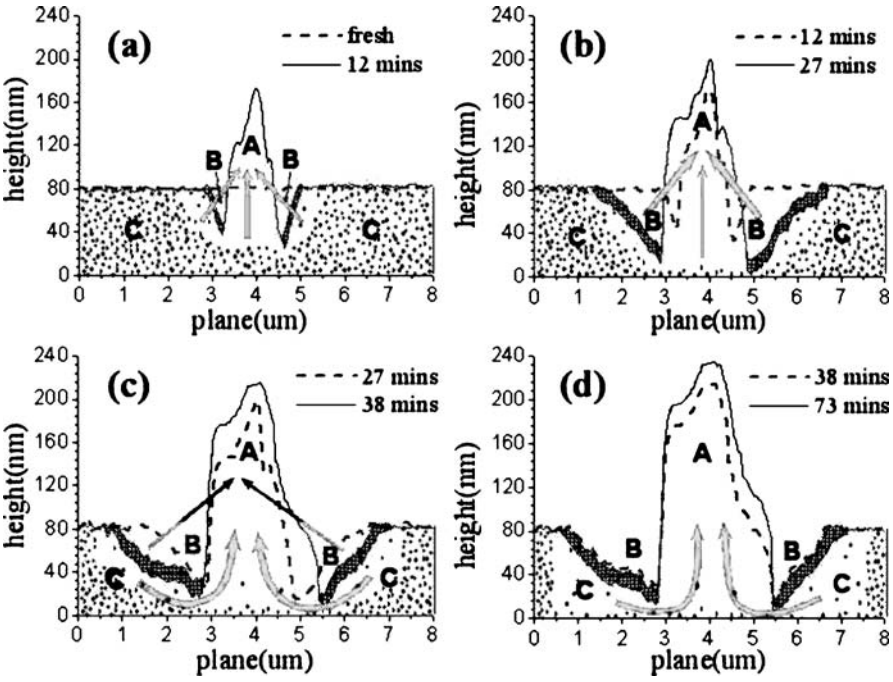


**Fig. 32.11.** Detailed morphology evolutions of thin MDMO-PPV/PCBM composite film upon thermal treatment. The *dots* represent PCBM molecules/nanocrystals and the density of the dots represents the richness of PCBM; the *diamond outlined regions* represent the depletion zones after PCBM material moved out for crystal growth, in which the density of the diamond outlines represents the richness of MDMO-PPV. (The sketches are similar to Fig. 5 in [36])

$R$ value ($R$ is the volume depletion/volume PCBM) for this period (Fig. 32.11b). With increased annealing time, the $R$ value rapidly decreases from its maximum. This behaviour reflects the fact that almost all the MDMO-PPV matrix film has collapsed; however, PCBM diffusion and crystal growth still continue (Fig. 32.11c). Finally, the diffusion rate of PCBM within the whole film decreases, reaching its equilibrium state, as shown in Fig. 32.11d.

The prominent morphology evolution of thin MDMO-PPV/PCBM films at elevated temperature is a typical phenomenon observed at various annealing temperatures (even as low as 60 °C for freestanding thin films), with different PCBM ratios in the composite and under various spatial confinements. This morphological change of the film is ascribed to the diffusion of PCBM molecules within the MDMO-PPV matrix even at temperatures below the glass-transition temperature of the MDMO-PPV matrix of about 80 °C and subsequent crystallization of PCBM molecules into large-scale crystals. However, for the high-performing PSC, the phase separation between electron donor and electron acceptor components should be controlled within a designed range to ensure a large interface for excitons to dissociate efficiently. Large-scale phase separation enormously reduces the size of this interface area, which causes significantly decreased performance or even leads to failure of the device. Therefore, large phase separation between donor and acceptor compounds should be prevented during both device fabrication and device operation, particularly at elevated temperature.

The purpose of annealing treatments, on the other hand, is to force re-organization of the active layer towards the desired film morphology as used in high-performance PSCs, in particular when one or all compounds of the bulk heterojunction have the ability to crystallize. One example is the system P3HT/PCBM as active layer for PSCs. The high efficiency of these devices can be related to the intrinsic properties of the two components. Regioregular P3HT self-organizes into a microcrystalline structure [38] and because of efficient interchain transport of charge carriers, the (hole) mobility in P3HT is high (up to approximately 0.1 $cm^2/V/s$) [39–41]. Moreover, in thin films interchain interactions cause a redshift of the optical absorption of P3HT, which provides an improved overlap with the solar emission. Also PCBM can crystallize, and control of nucleation and crystallization kinetics allows the adjustment of the crystal size [37]. However, continuous crystallization may result in single crystals with micrometre sizes, which is not beneficial for efficient exciton dissociation, as discussed above.

Interestingly, the efficiency of solar cells based on P3HT and fullerenes was shown to depend strongly on the processing conditions and to be improved particularly by a thermal annealing step (Fig. 32.12) [26, 42, 43]. It was demonstrated that crystallization and demixing induced by the thermal annealing controls the nanoscale organization of P3HT—which forms long nanowires—and PCBM in the photoactive layer towards a morphology in which both components have a large interfacial area for efficient charge generation, have attained crystalline order that improves charge transport, and form continuous paths for charge transport to the respective electrodes (Figs. 32.12, 32.13). We infer that the long, thin fibrillar crystals of P3HT in a homogeneous nanocrystalline PCBM layer are the key to the high device performance, because they are beneficial for charge transport and control the degree of demixing [16].

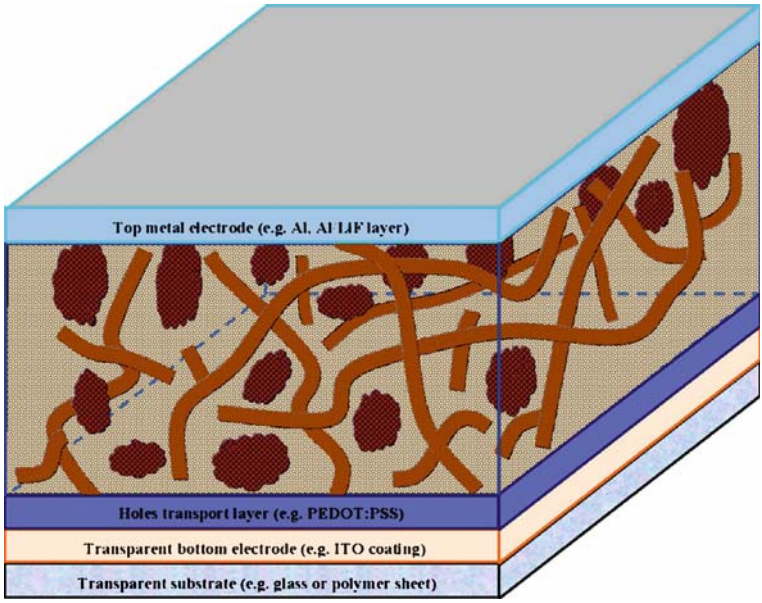


**Fig. 32.12.** The interpenetrating network in the active layer composed of P3HT and PCBM established after annealing

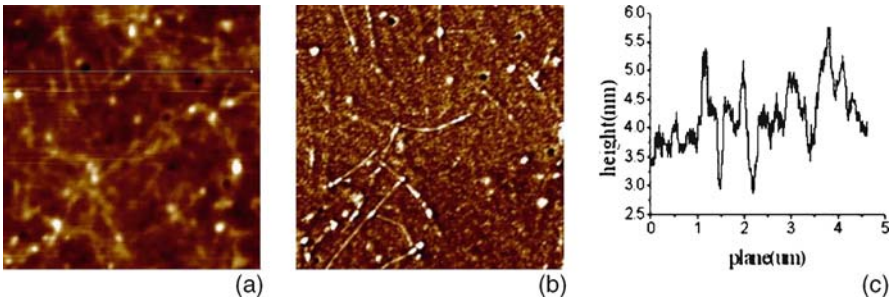


**Fig. 32.13.** AFM height images (**a**), phase image (**b**) and corresponding cross-section (**c**) of P3HT/$C_{60}$ (PCBM-like) blends; scan size 5 × 5 $\mu m^2$

Another aspect related to annealing experiments is reorganization with or without confinement of the active layer of PSCs, i. e. annealing performed with or without a top electrode. It is well known that especially for thin films the conformation of polymer chains on the surface or at interfaces may differ from that in the "bulk" state. It is recognized that a very thin layer is present on the surface of thin polymer films, in which tie molecules are enriched and therefore the local free volume is high and chain aggregation becomes loose [44, 45]. Moreover, the presence of surfaces/interfaces influences the organization and reorganization of thin-film samples. It has been shown that, depending on the type of confinement of the active layer, the morphology evolution of MDMO-PPV/PCBM composite films is different upon

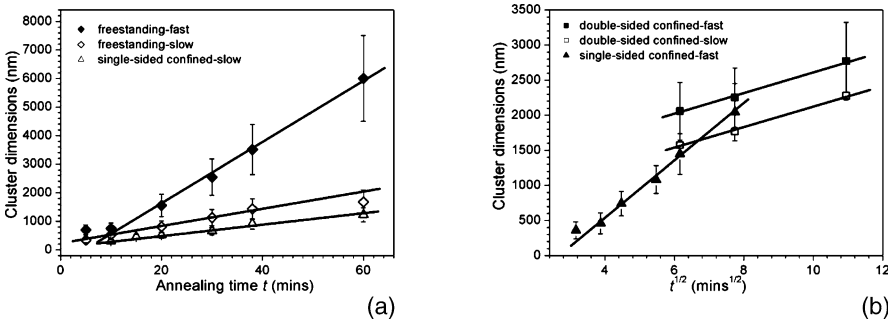


**Fig. 32.14.** Growth rates of PCBM single crystals from thin blend films with MDMO-PPV annealed at 130 °C for various conditions of confinement. **a** Growth rate versus annealing time $t$ in the fast (*closed diamonds*) and slow (*open diamonds*) growth directions of the PCBM crystals for the freestanding film and in the slow (*triangles*) growth direction for the single-sided confined film. **b** Growth rate versus $t^{1/2}$ in both the fast (*closed squares*) and slow (*open squares*) growth directions for the double-sided confined film and in the fast (*triangles*) growth direction for the single-sided confined film. The *solid lines* are the linear fittings. (Reprinted with permission from [46]. Copyright 2005 American Chemical Society)

thermal annealing (Fig. 32.14) [46]: for no confinement, which corresponds to freestanding films that most of the time are used for TEM investigations, or single-sided confinement, in which the films are deposited on a substrate (common situation for AFM investigations), large elongated PCBM single crystals are formed. In case of double-sided or sandwichlike confinement (situation in the final device), in which the deposited films are additionally covered by a top layer, the top electrode, the low mobility of PCBM results in diffusion rate dominated and slow growth of PCBM crystals within the layer. As a consequence, the kinetics of phase segregation upon thermal annealing for the double-side confined thin film is slower than that in freestanding films or substrate-supported films [46]. This suppressed kinetics of phase separation could benefit the performance and stability of PSCs. However, one bears the risk of interface damage resulting from relaxation of polymer chains in the thin film, or dewetting between the photoactive layer and the metal contact if the thermal annealing is performed with the presence of a top-metal layer. These results demonstrate that annealing at different stages in device processing may result in different morphologies of the active layer, and thus in different performance of the final device.

### 32.3.3 All-Polymer Solar Cells

One of the main drawbacks of PSCs based on polymer/PCBM photoactive layers is the high amount of PCBM required for charge carrying; a large amount of PCBM (50–80 wt%) is required to form networks for charge transport to the electrode. Unfortunately, because of its symmetrical molecular architecture, PCBM contributes only insignificantly to light absorption. In contrast, polymer/polymer or so-called all-polymer solar cells have the specific advantage that both compounds

are able to absorb light. By tuning the molecular architecture of the polymer, like by substitution of ligands, a broad absorption range can be achieved, even reaching the IR region. A few examples of such blends are known from the literature, e. g. a blend of a poly(phenylenevinylene) derivative (MEH-PPV) with the corresponding cyano-substituted variant (CN-PPV) of this polymer, or a blend of p-type and n-type fluorine derivatives [11, 12, 20, 47–50]. In general, all the above-discussed processing parameters influencing morphology formation are also valid for all-polymer systems: solvent used, evaporation rate, compound ratio and concentration in the solution, as well as annealing. Moreover, by choosing the proper synthesis route, one can tailor the molecular weight and branching of the polymers so that processability as well as device performance are improved. After optimization of the polymer architecture as well as the processing conditions for such all-polymer solar cell systems, recently, power conversion efficiencies of about 1.5% have been reported [51].

For the system MDMO-PPV/PCNEPV dewetting of the active layer on PEDOT-PSS has been identified by AFM studies to be an important feature influencing the morphology formation during processing. In AFM height-contrast images of the MDMO-PPV/PCNEPV blend after spin-coating onto PEDOT-PSS-coated glass substrates, the appearance of the film is rather heterogeneous, and large regions with different contrast can be distinguished. As revealed by AFM investigations of the topography of the blend layer and by corresponding thickness maps obtained by energy-filtered TEM (EFTEM), dewetting of PCNEPV with the substrate might cause these thickness variations, and a homogenized active layer only can be created through subsequent annealing [52].

To prove this assumption, we investigated the interface between PEDOT-PSS and the MDMO-PPV/PCNEPV layer; a float-off technique was used to remove the polymer layers from the glass/ITO substrate. By doing so, the PEDOT-PSS layer dissolved and the photoactive layer floated on the water. It is assumed that this procedure does not alter the morphology of the active layer. The backside of the pristine polymer blend film was surprisingly rough; patterns in the form of a network and dropletlike structures were found (Fig. 32.15). This structure is attributed to dewetting of the photoactive blend on top of the PEDOT-PSS layer. To rule out the presence of PEDOT-PSS left after floating, we also probed films that were peeled from the substrate, and these surfaces yielded similar AFM images. Further, we note that the spin-coated PEDOT-PSS layer is flat (rms roughness less than 2 nm) and consequently does not act as a mould for the observed rough layer. The height of the structures is about 12 nm, which is considerable compared with the 40-nm thickness of the measured film.

The backsides of films annealed on PEDOT-PSS were completely flat (rms roughness less than 2 nm). Moreover, temperature-dependent AFM experiments on (initially pristine) films revealed the disappearance of the dewetting structure at about 70 °C. Blends spun on bare glass substrates do not show this dewetting behaviour and form immediately flat films. The same holds for films of the pure materials (MDMO-PPV or PCNEPV) on either PEDOT-PSS or glass, which proves the assumption that dewetting of the active layer onto PEDOT-PSS causes the heterogeneous film morphology, and thus a low efficiency of the corresponding device. After annealing, fortunately, one observes considerable efficiency increase.

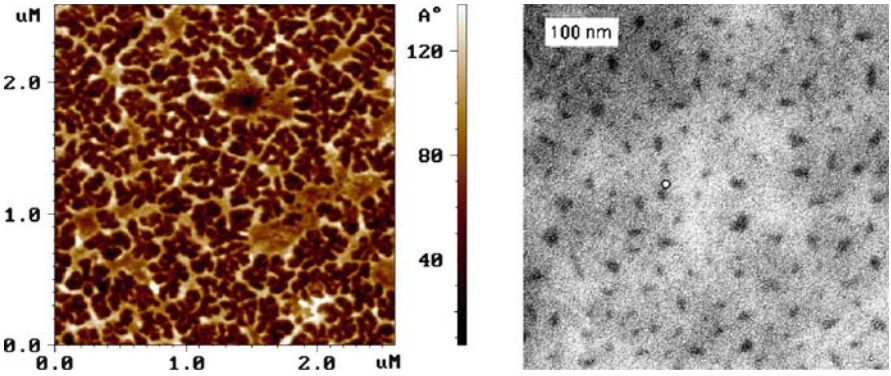


**Fig. 32.15.** *Left*: AFM height-contrast image of the interface between the MDMO-PPV/PCNEPV active layer and the PEDOT-PSS layer showing high roughness probably caused by dewetting. *Right*: Energy-filtered transmission electron microscopy image showing the homogeneous phase separation after annealing (*black dots* correspond to PCNEPV domains, and *brighter matrix* corresponds to MDMO-PPV; more details on the phase separation of this system can be found in Sect. 32.4.2). (Reprinted with permission from [20], copyright 2004 American Chemical Society, and [52], copyright 2005 Wiley)

## 32.4 Nanoscale Characterization of Properties of the Active Layer

### 32.4.1 Local Optical Properties As Measured by Scanning Near-Field Optical Microscopy

As for the system MDMO-PPV/PCBM, the system P3HT/PCBM may show in certain circumstances large-scale phase segregation of PCBM. Better understanding of such diffusion features of PCBM is required to control phase segregation towards the desired morphology, which ultimately offers good device performance. Thus, in the following we demonstrate that the application of SNOM is able to provide insights related to such features.

In a near-field optical measurement a single-mode optical fibre with a hole of around 100 nm in diameter on the sharp end is placed into the near field (distance of 2–4 nm) of the sample investigated. A near-field probe generates an evanescent field, the wavelength of which is shorter than that of the propagating field and thus the diffraction limit of around one half of the wavelength of the source light is circumvented [53]. The spatial resolution is then defined by the diameter of the hole. High-quality optical contrast images were obtained by this technique. It is especially important for analysis of materials on the nanometre scale. As an example, in a recent SNOM study properties of MEH-PPV/PCBM systems were studied [54].

Near-field microscopic measurements provide a range of information about the P3HT/PCBM films studied [55]. In Fig. 32.16 a topography contrast image and the corresponding cross-sectional plot are shown. Different grey levels are consistent with the height of the features as can be seen from the corresponding cross-sectional plot. Three different regions can be distinguished in the sample: (1) a bright crystalline feature sticking out of the film plane and having a size of about 20 μm in

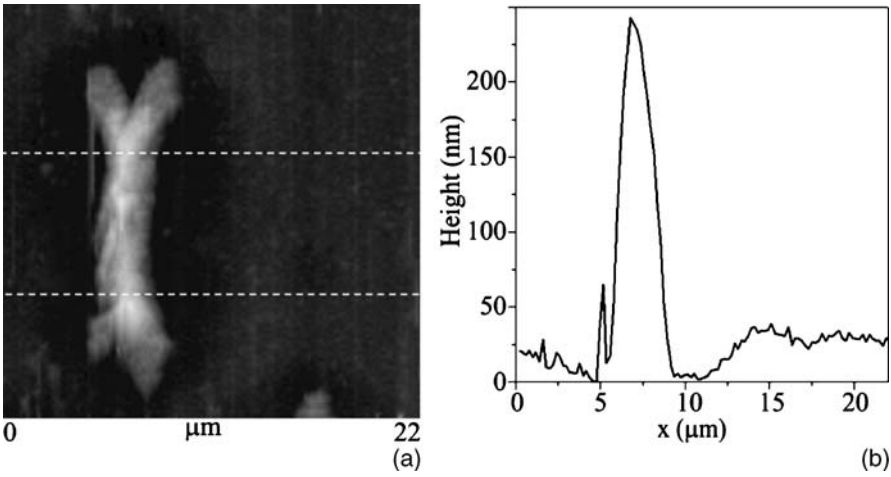


**Fig. 32.16.** Topography image (**a**) and average profile of selected area (**b**) obtained from scanning near-field optical microscopy (SNOM) measurements. (Reprinted with permission from [55]. Copyright 2004 American Chemical Society)

length and 5 µm in width, and a typical height of about 200 nm; (2) a dark zone surrounding this crystal; and (3) the remaining area representing the initial film plane. From the cross-sectional plot, we see that the zone surrounding the crystal is substantially deeper when compared with the initial film plane having a depth on the order of 30–50 nm, which is a first indication for depletion of PCBM similar to in the MDMO-PPV/PCBM system [14].

Optical contrast SNOM images taken in transmission mode are shown in Fig. 32.17. The images were acquired at two different radiation wavelengths and show different contrast behaviour. For our experimental setup, simultaneously topography and light absorption measurements with a He–Ne laser of wavelength 632.8 nm were performed. Figure 32.17a shows the optical absorption image of the same area as in Fig. 32.16a. For irradiation with such laser light the area with smaller thickness surrounding the crystal demonstrates a higher absorbance value compared with that of the initial film. However, at a wavelength of 532 nm the absorbance behaviour inverts: the absorbance of the initial film exceeds the absorbance of the crystal-close region. The crystals themselves have comparable transmission at both the 632.8- and 532-nm wavelengths. Unfortunately, our experimental setup does not allow simple change of the laser source, so we were not able to perform the optical absorption measurement on the same sample area.

These differences in optical absorption can be explained by monitoring the absorption spectra of pure P3HT and a 1:1 by weight P3HT/PCBM mixture obtained using a conventional UV–vis spectrometer (Fig. 32.18). After mixing the P3HT with PCBM, the absorption maximum in the visible spectrum shifted from 570 nm to shorter wavelengths. Assuming that the areas surrounding the PCBM crystals are depleted of PCBM, we can explain the different absorption characteristics depending on the irradiation wavelength used. For both wavelengths, maximum absorption is found for the pure PCBM crystals, which mainly is related to their large thickness

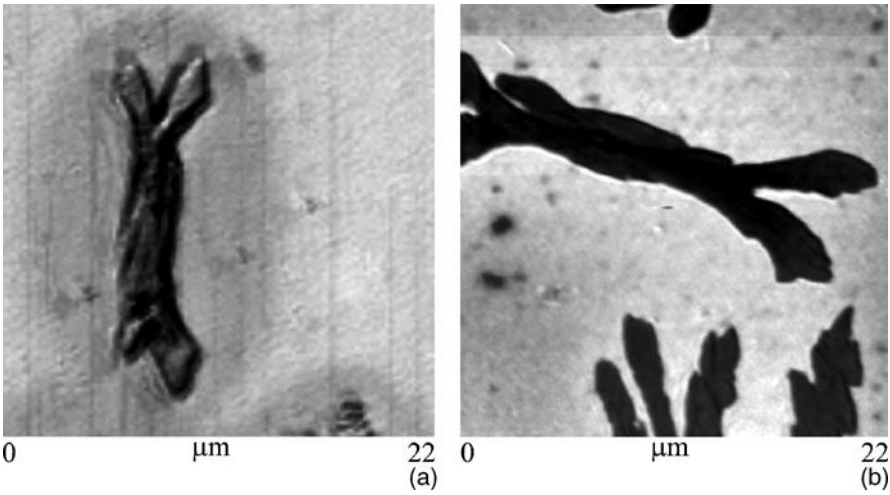


**Fig. 32.17.** Optical contrast images obtained in SNOM transmission mode using monochromatic laser radiation with wavelengths of 632.8 nm (**a**) and 532 nm (**b**). (Reprinted with permission from [55]. Copyright 2004 American Chemical Society)

**Fig. 32.18.** UV–vis absorption spectra in the visible region of pure P3HT and its 1:1 by weight mixture with PCBM. (Reprinted with permission from [55]. Copyright 2004 American Chemical Society)

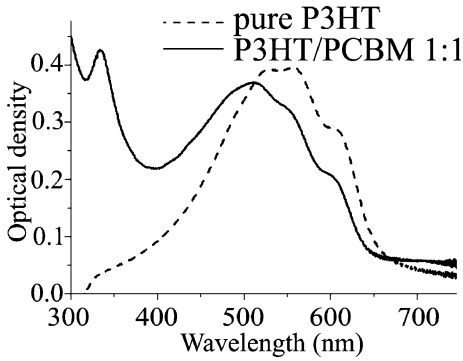


of several hundreds of nanometres. Comparing the initial film area, still composed of 1:1 P3HT/PCBM, with the area probably depleted by PCBM, the relatively higher absorption of 632.8-nm irradiation of the latter is related to the dominantly larger absorption of pure P3HT for such a wavelength. In contrast, the slight higher absorption of the initial film for 532-nm irradiation is caused by the somewhat similar absorption characteristics of pure P3HT and the P3HT/PCBM mixture for such a wavelength; however, the depletion zone is thinner and thus results in less total absorption.

### 32.4.2 Characterization of Nanoscale Electrical Properties

In general, performance measurements of PSCs are carried out on operational devices having at least the size of square millimetres to centimetres. On the other hand, the

characteristic length scale determining the functional behaviour of the active layer is on the order of 10 nm (exciton diffusion length) to about 100 nm (layer thickness). Moreover, it is believed that the local organization of nanostructures dominantly controls the electrical behaviour of devices. Thus, it is necessary to obtain property data of nanostructures with nanometre resolution to be able to establish structure–property relations that link length scales from local nanostructures to large-scale devices.

In this respect, a very useful analytical technique is SPM. In previous studies, scanning tunnelling microscopy (STM) was used for investigation of semiconducting polymers [56–58]. In particular, the current–voltage ($I$–$V$) characteristics at the surface of PPV samples have been studied and modelled. However, in STM measurements, variations of the topography and information on the electrical behaviour are superimposed, and especially for electrically heterogeneous samples like bulk heterojunctions, separation of electrical data from topography information is difficult. Other SPM techniques probably better suited for analysis of the local functionality of polymer semiconductors are SNOM and AFM. Near-field optical microscopy and spectroscopy has been used, e. g., to study aggregation quenching in thin films of MEH-PPV [57]. The results obtained suggest that the size of aggregates in thin films must be smaller than the resolution limit of SNOM, roughly 50–100 nm. Further, SNOM has been applied to map topography and photocurrent of the active layer of some organic photovoltaic devices [59]; however, the spatial resolution reported in that study was only about 200 nm. Our results, as reported earlier, show a similar lateral resolution of about 100 nm.

One of the electrical methods of AFM is scanning Kelvin probe microscopy (SKPM), which is used to obtain the distribution of potentials at the sample surface. In fact, SKPM determines the difference between the work function of the tip and the sample surface. Measuring inside a glove box allows us to reduce the influence of adsorbed water on the surface potential measurements. We have used gold-coated tips to measure surface potential variations within MDMO-PPV/PCNEPV blends. The surface potential distribution image obtained (Fig. 32.19) shows that the work

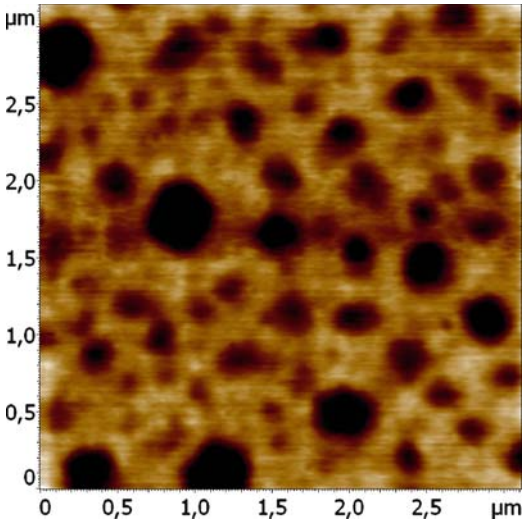


**Fig. 32.19.** Surface potential distribution measured with an Au-coated tip on a 3.1 × 3.1 $\mu m^2$ area of a MDMO-PPV/PCNEPV blend sample. The measured colour scale corresponds to a difference of 80 mV

function of the domains is different from the work function of the matrix, which proves the existence of phase separation inside the active layer. The difference in surface potential between domains and matrix of the sample is up to 0.12 V. Since morphology influences the measured potential, absolute determination of the work function of the components in the blend is difficult [60]. The lateral resolution of SKPM is about 50 nm [61].

AFM using a conductive probe, so-called C-AFM [62, 63], is able to overcome the abovementioned problem of STM and provides a higher spatial resolution than SNOM. Because AFM uses the interaction force between the probe and the sample surface as a feedback signal, both topography and conductivity of the sample can be mapped independently. Theoretically, the resolution of C-AFM is as small as the tip–sample contact area, which can be less than 20 nm. C-AFM is widely used for the characterization of electrical properties of organic semiconductors. For example, single crystals of sexithiophene have been studied [64], where the $I$–$V$ characteristics of the samples were measured. Several electrical parameters, such as grain resistivity and tip–sample barrier height, were determined from these data. In another study, the hole transport in thin films of MEH-PPV was investigated and the spatial current distribution and $I$–$V$ characteristics of the samples were discussed [22].

As mentioned above, for analysing our active layer samples by means of C-AFM, we operate the atomic force microscope in a glove box to protect the samples from degeneration. It is well known that the performance of most PSCs as well as of organic electronic systems, in general, drops dramatically after short-time exposure to oxygen, especially when they are illuminated by light [65]. In contrast to characterization of whole devices in an inert atmosphere, C-AFM measurements are commonly performed, however, in air at ambient conditions. It is the purpose this section to clearly demonstrate that the local electrical properties of nanostructures in the active layer of PSCs are changed for several reasons when C-AFM measurements are performed at ambient conditions; and as a consequence the results obtained are not comparable with data gained from device characterization. At the same time, we would like to illustrate that C-AFM measurements performed in the inert atmosphere of a glove box provide reliable information on electrical properties of organic nanostructures and allow the creation structure–processing–property relations of functional polymer systems.

MDMO-PPV/PCBM is one of the systems best studied for applications as an active layer in high-efficiency PSCs; efficiencies of about 2.5% have been reported for optimized preparation conditions [66]. Further, it has been demonstrated that the performance of devices having these compounds as a blend in their active layers decreases immediately when they are exposed to air [67]. For this reason, we chose the blend MDMO-PPV/PCBM as a model system for our C-AFM experiments.

Figure 32.20 shows a series of C-AFM images obtained at ambient conditions in air of a thin PCBM/MDMO-PPV film spin-coated from toluene solution. All images were acquired with a tip coated with a gold layer. For such preparation conditions, PCBM and MDMO-PPV segregate, and PCBM forms large nanocrystalline domains imbedded in the MDMO-PPV matrix [14, 68]. The topography image (Fig. 32.20a) shows that the PCBM domains (bright areas) have maximum diameters of about 500 nm. Phase segregation is responsible for the high roughness of the film: the PCBM domains stick a few tenths of a nanometre out of the film plane.

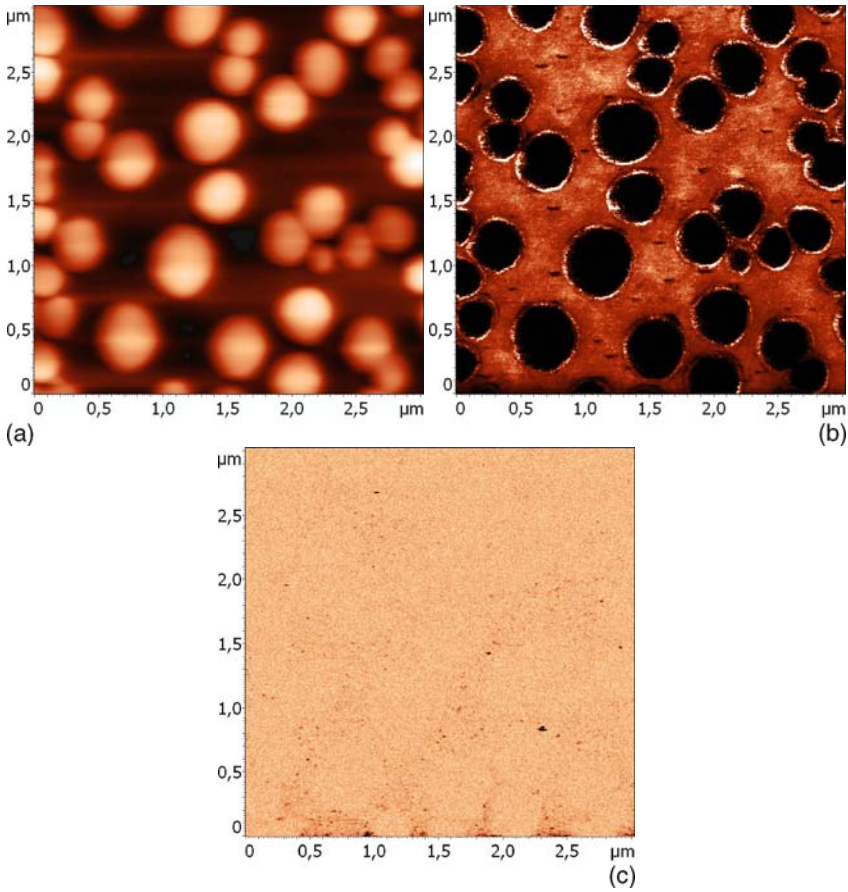


**Fig. 32.20.** Conductive AFM (C-AFM) image series acquired at ambient conditions in air of a thin PCBM/MDMO-PPV film spin-coated from toluene solution: **a** topography image (colour scale represents 70-nm height variations), and current distribution images of the same area for **b** a negative bias at the tip of −2.3 V (colour values represent 1.2-nA current variation) and for **c** a positive bias at the tip of +10 V (colour values represent 250-pA current variation)

Figure 32.20b and c represents the current distribution image for bias voltages at the tip of −2.3 V (Fig. 32.20b) and +10 V (Fig. 32.20c), respectively, measured at the same sample area as the topography image. For negative bias, good contrast is obtained between the electron donor (p-type semiconductor) and the electron acceptor (n-type semiconductor) materials in the sample. From the corresponding energy level diagram (Fig. 32.21) it follows that the difference between the HOMO level of MDMO-PPV and the Fermi levels of both electrodes (ITO/PEDOT-PSS and the Au tip) is rather small, so we expect ohmic contacts for hole injection and strong energy barriers for electrons [21, 64]. Therefore, a hole-only current through the MDMO-PPV is expected for both polarities of voltage in an ITO/PEDOT-PSS/MDMO-PPV/Au-tip structure. On the other hand, we can conclude that areas

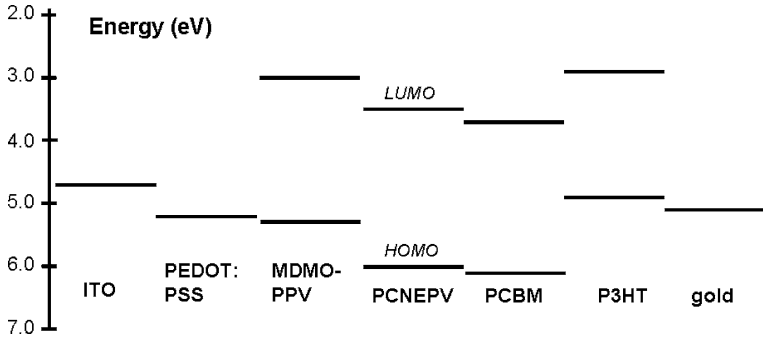


**Fig. 32.21.** Energy level diagram for a few materials commonly used in polymer solar cells. *HUMO* highest occupied molecular orbital, *LUMO* lowest unoccupied molecular orbital

of low current level correspond to the electron-acceptor materials, i. e. PCBM, which is in accordance with the abovementioned topographical observations. For positive bias, however, no differences between the two phases can be obtained, and the measured overall current level is below the noise level of our experimental setup.

Since the compounds under investigation are sensitive to oxygen and at ambient conditions the always-present water layer on top of the sample surface interferes with nanometre-scale electrical measurements, which has been reported recently for the case of surface potential measurements [69], we performed additional C-AFM experiments on the same MDMO-PPV/PCBM system but in an inert atmosphere. We assembled the C-AFM setup in a glove box filled with a nitrogen atmosphere and an oxygen and water level below 1 ppm.

Figure 32.22 presents C-AFM measurements of such a MDMO-PPV/PCBM thin-film sample. The main difference is that the sample was sealed in a vessel after preparation in another glove box, and was subsequently transported to and mounted in the C-AFM setup assembled in a glove box. This procedure guarantees that the sample is not exposed to oxygen or water, and imitates the common procedure of handling devices in an inert atmosphere. For the negative bias of $-10$ V similar features as discussed for Fig. 32.20b can be seen (Fig. 32.22a). The dark areas represent PCBM domains with low current imbedded in the bright MDMO-PPV matrix showing high current. The current level scaling of the image of about 20 nA is larger than for Fig. 32.20b because of the higher bias applied, and probably the different contact load of the tip on the sample surface. In contrast to measurements performed in air, also for the positive bias of $+10$ V good contrast between the two phase-segregated compounds can be obtained (Fig. 32.22a). Besides some little drift of the area probed during the two successive C-AFM measurements with positive and negative biases, PCBM domains can be recognized as dark areas embedded in the bright MDMO-PPV matrix. The current level scaling of the image is lower as for the case of positive bias; however, the higher noise level results in a larger total current level scaling of about 20 nA. These results demonstrate the importance of performing C-AFM analysis in an inert and oxygen-free and water-free atmosphere to protect samples from degeneration and to save their full functionality for reliable data sets.

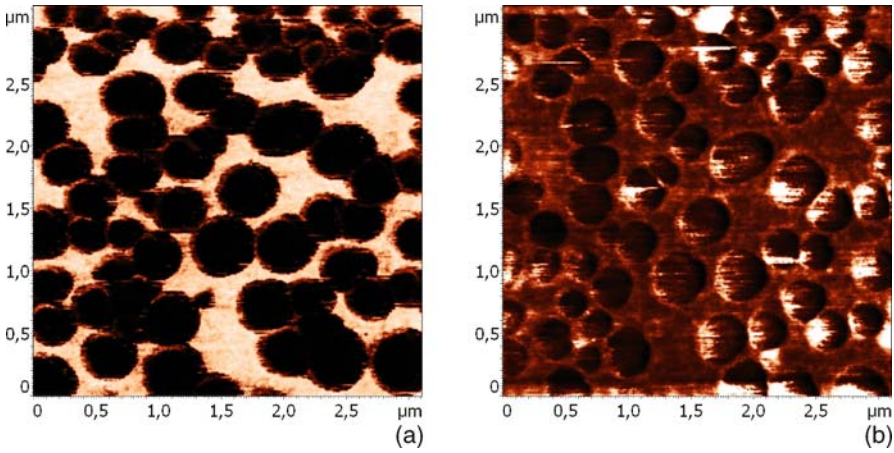


**Fig. 32.22.** C-AFM images of a PCBM/MDMO-PPV thin film sample acquired in the inert and water-free atmosphere of a glove box showing the current distribution of the same sample area for **a** a positive bias at the tip of +10.0 V (colour values represent 18-nA current variation) and for **b** a negative bias at the tip of −10 V (colour values represent 20-nA current variation)

On the basis of these results, recently the first study on the spatial distribution of electrical properties of realistic bulk heterojunctions was performed by applying C-AFM with lateral resolution better than 20 nm [70]. For this study the MDMO-PPV/PCNEPV system was chosen. Measurements of the electrical current distribution over the sample surface were performed with a Au-coated tip. Again, in such an experiment the tip plays the role of the back electrode but having a much more localized contact area. A voltage was applied to the tip and the ITO front electrode was grounded (Fig. 32.5). For C-AFM measurements the tip was kept in contact with the sample surface while the current through the tip was measured. In contrast to operation in intermittent-contact mode, contact mode is characterized by a strong tip–sample interaction that can lead to destruction of the surface, especially in the case of soft polymer samples. Therefore, the load applied to the tip during C-AFM has to be small enough to reduce sample destruction and, at the same time, it must provide a reliable electric contact. We usually operated with a load of about 10–20 nN. The contact cantilevers used for C-AFM are suitable for operation in intermittent-contact mode as well as in contact mode, so nondestructive testing of the sample surface could be performed before and after the C-AFM measurements. C-AFM measurements of the same sample area were done several times and resulted in completely reproducible data. Subsequent analysis of the surface performed in intermittent-contact mode showed almost no destruction of the sample surface; only minor changes were detected from time to time.

A topography image and the corresponding current distribution measured at +8 and −8 V on the tip are shown in Fig. 32.23. All images were acquired subsequently, so some drift occurred. All pronounced domains in the topography image (Fig. 32.23a) correlate with regions of minimal current in the C-AFM image (dark areas in Fig. 32.23b).

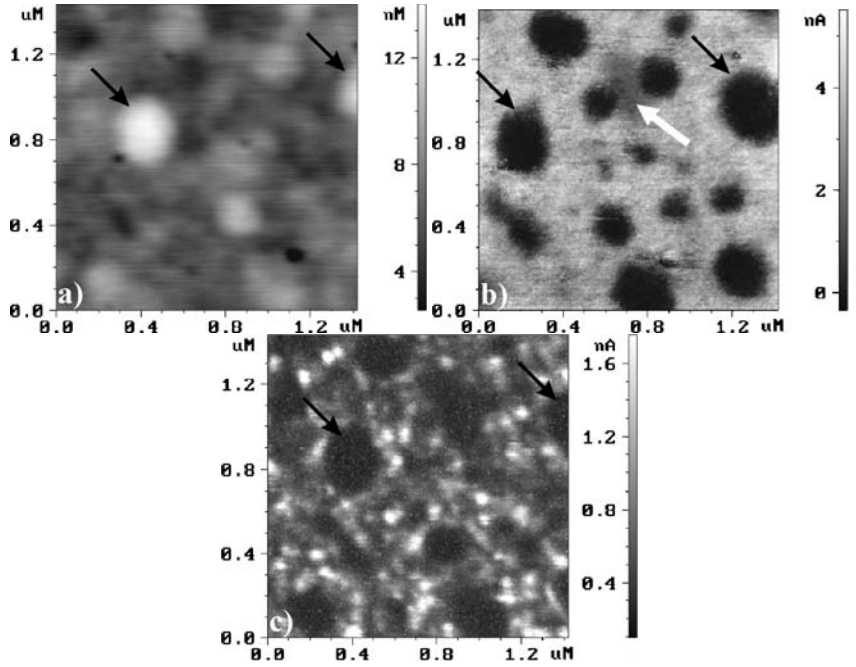


**Fig. 32.23.** C-AFM images of the same area of a MDMO-PPV/PCNEPV active layer: **a** topography, **b** current distribution image with a positive bias at $U_{\text{tip}} = +8$ V( the *white arrow* in **b** indicates a domain with reduced current) and **c** current distribution image with a negative bias at $U_{\text{tip}} = -8$ V. *Black arrows* indicate the same domains for reason of easy identification. (Reprinted with permission from [70]. Copyright 2006 Elsevier)

From the corresponding energy level diagram (Fig. 32.21), it follows that the difference between the HOMO level of MDMO-PPV and the Fermi level of both electrodes is rather small, so we expect ohmic contacts for a hole injection and strong energy barriers for electrons. Therefore, a hole-only current through the MDMO-PPV is expected for both polarities of voltage in an ITO/PEDOT-PSS/MDMO-PPV/Au-tip system. The energy difference between the HOMO and the LUMO of PCNEPV and the Fermi levels of both electrodes is about 1 eV, which means that a large barrier for electron injection exists in the structure ITO/PEDOT-PSS/PCNEPV/Au tip (some changes of barrier heights are possible when contact between metal electrodes and organic material occurs [21, 64]). Because the hole mobility of an n-type polymer is typically smaller than that of a p-type polymer, a hole-only current through the MDMO-PPV is larger than for PCNEPV in both bulk and contact-limited regimes. Therefore, we assume that the observed contrast in Fig. 32.23b is due to a hole current, flowing through the MDMO-PPV-rich phase (see also Fig. 32.15, EFTEM image of a comparable system).

However, C-AFM measurement also shows regions with a current value lying between that of the MDMO-PPV matrix and the PCNEPV domains. An arrow in Fig. 32.23b marks one of these regions. These areas might be assigned as PCNEPV domains inside the active layer that are possibly covered by MDMO-PPV.

It has been reported that the electrical contrast measured by C-AFM at the surface of samples depends on the sign of the voltage applied [64]. As shown in Fig. 32.23c, the C-AFM measurements at negative bias on the tip showed drastic changes of the contrast in the current images compared with positive bias (Fig. 32.22b). PCNEPV domains again showed only little current at low load; however, MDMO-PPV showed a heterogeneous spatial current distribution. These electrical heterogeneities indicate small grains with a typical size of 20–50 nm, which differs depending on the value of current. A similar structure was observed on MEH-PPV films [22]. In the case of MEH-PPV, the authors attribute these substructures to a special and very local organization of the film that could be caused by local crystallization of stereoregular parts of the MEH-PPV molecules or by impurities incorporated during the synthesis.

In addition to topography and current-sensing analysis, current-imaging spectroscopy was performed as well. The procedure for such measurements is similar to the so-called force volume technique [71], which implies measurements of the force–distance curve at each point of a scan in order to get complete information about lateral distribution of mechanical properties at the surface. Here, we extend this method to measurements of electrical properties of the sample [72]. Current–distance ($I$–$z$, at constant voltage) and current–voltage ($I$–$V$, for constant distance; always in contact) dependencies were collected at each point of a scan. The procedure for such measurements is shown schematically in Fig. 32.24.

An array of $128 \times 128$ $I$–$z$ curves at $+8$ V on the tip was obtained in order to study the influence of the applied load on the distribution of current. An $I$–$z$ curve at one point was obtained by movement of the tip by the scanner in the $z$-direction. In our experiment first we bring the tip in contact with the sample surface, then the scanner with the attached tip is moved up 60 nm, and finally moves down for 160 nm while simultaneous measurements of the local current are performed (Fig. 32.25). The change of the $z$-position of the scanner, when tip–sample contact occurs, leads to both the bending of the lever and penetration of the tip in the sample. Additional experiments showed that the penetration depth in the range of the load used is much smaller than lever bending, i. e. the load can be roughly estimated from the $z$ movement of the scanner: $F = k\Delta z$ , where $k$ is the cantilever force constant and $\Delta z$ is the scanner displacement calculated from the first point where tip–sample contact occurs. The cross-section of the array of $I$–$z$ curves obtained shows the distribution of the current at the sample surface for a certain $z$-position of the scanner (or load). Movement from point to point was executed in contact mode under small load (less than 20 nN in our experiments). As a result the destructive action of the lateral force is reduced significantly. It is also possible to perform such measurements in intermittent-contact mode, thus making the measurements of polymer topography

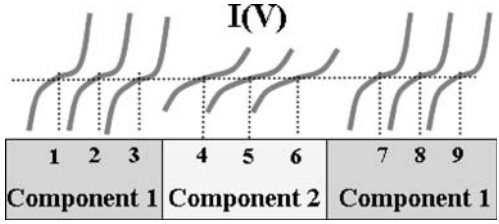


**Fig. 32.24.** $I$–$V$ measurements at nine consecutive points. The *light blue area* represents a PCNEPV-rich domain, the *beige areas* the MDMO-PPV-rich matrix

more precise. For the sample studied here, we obtained similar results with current imaging spectroscopy performed in both contact and intermittent-contact mode.

Figure 32.25 demonstrates $I$–$z$ curves measured in the PCNEPV domains and the MDMO-PPV matrix. For loads in the range 10–30 nN the current is approximately constant, but for an increased load of more than 30 nN the current starts to rise rapidly. In the case of PCNEPV a similar trend could be measured; however, because PCNEPV is a less good hole conductor, current values are on a lower level compared with MDMO-PPV. This probably means that current measurements on PCNEPV need a greater tip–sample interaction compared with those on MDMO-PPV. Even a strong penetration of the sample surface by the tip may be required.

In contrast, Fig. 32.26 shows the typical $I$–$V$ behaviour of this system, and the corresponding C-AFM current distribution images for various biases when they are measured in an inert atmosphere. The data were obtained by application of so-called $I$–$V$ spectroscopy, which means that for a matrix of 128 × 128 points on the surface of the sample full $I$–$V$ curves were measured for biases from −10 to +10 V. Three different types of $I$–$V$ characteristics can be found in the sample depending on the location of the measurement. For domains of the electron-acceptor compound PCNEPV (see corresponding EFTEM data, Fig. 32.15b) the current is always low, and the general contrast of the current distribution images depends only on the bias applied. In the case of the electron-donor matrix compound MDMO-PPV two different $I$–$V$ characteristics can be obtained showing almost the same behaviour for positive bias but varying significantly for negative bias. The current distribution images of Fig. 32.26 demonstrate this behaviour and provide additional information about lateral sizes of the MDMO-PPV heterogeneities. The point resolution of the images is about 15 nm. Some heterogeneities can be recognized with sizes as small as about 20 nm as follows from C-AFM measurements (Fig. 32.23). The origin of the heterogeneities in MDMO-PPV still is under investigation; however, it is assumed that either small crystalline domains are formed or impurities originating from the synthesis process are detected. The C-AFM results obtained on pure MDMO-PPV film are identical to that obtained on the matrix in the heterogeneous film MDMO-

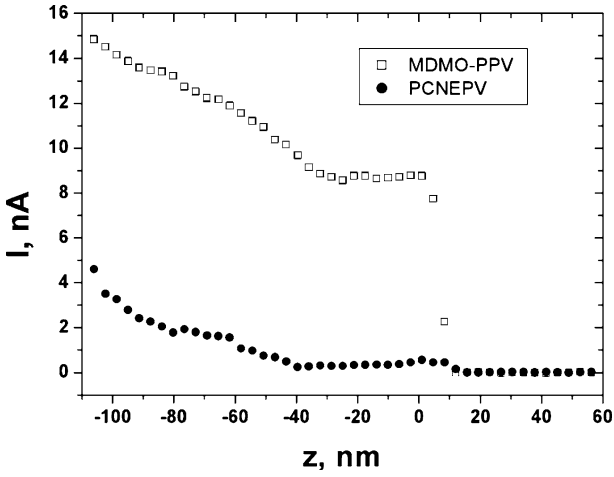


**Fig. 32.25.** Current–distance behaviour of the MDMO-PPV matrix and PCNEPV domains. The direction from right to the left corresponds to the approaching of the tip to the substrate surface. (Reprinted with permission from [70]. Copyright 2006 Elsevier)

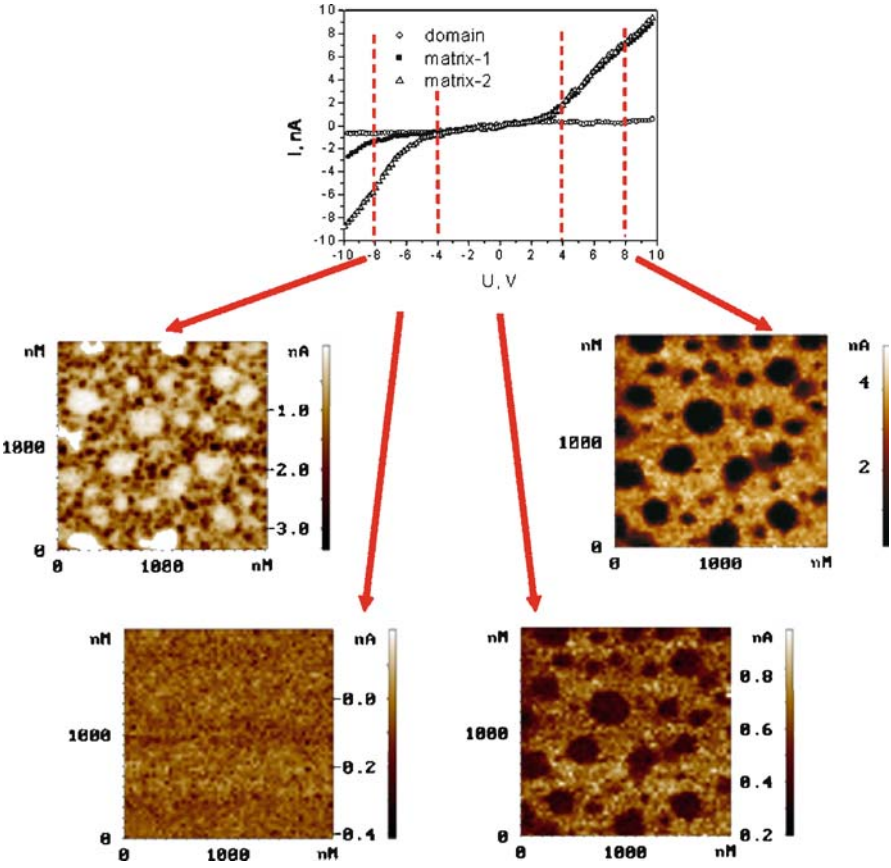


**Fig. 32.26.** *Top*: Typical $I$–$V$ curves as measured for each point of the $I$–$V$ spectroscopy scan (128 × 128 pixels) demonstrating the heterogeneous $I$–$V$ characteristics of the MDMO-PPV matrix. *Bottom*: For four biases the corresponding current distribution images are shown demonstrating the obvious contrast between PCNEPV and MDMO-PPV for high bias as well as contrast within the MDMO-PPV matrix with heterogeneities as small as a few tens of nanometres

PPV/PCNEPV. The log $I$–log $V$ plot of data obtained shows quadratic dependence of the current $I$ on the voltage $V$ measured on MDMO-PPV. This implies space-charge-limited current that is in agreement with $I$–$V$ measurements on complete devices [73, 74].

## 32.5 Summary and Outlook

PSCs with photoactive layers based on compounds forming intermixed bulk heterojunctions are becoming more and more attractive for commercial application. In this respect, one key aspect for high-performance devices is fundamental knowledge of

structure–processing–property relations, on the nanometre length scale. Intensively, studies have been performed on the influence of solvent used, the composition of the solutions, thin-film preparation conditions, crystallization behaviour and post-treatments, to name but a few, on the functional properties of the photoactive layer. Nevertheless, our insights into features influenced by the local organization of functional structures, such as the interface organization at the junctions between phases, are sparse and need improvement. Only with the availability of such data, novel approaches for further improving and designing the morphology of the bulk heterojunction photoactive layer can be developed.

Currently, by choosing the optimum solvent, compound composition and preparation conditions nanoscale phase separation between electron-donor and electron-acceptor constituents can be achieved, and continuous pathways for charge carriers to the electrodes are provided. However, from theoretical considerations the efficiency of PSCs should reach at least 10%, which is twice the highest efficiency reported recently. Such performance would make PSCs commercially very attractive and comparable with amorphous silicon solar cells, but having the strong advantage of easy processing. So, we constantly have to continue closing our knowledge gaps on structure–processing–property relations on the nanoscale to ultimately reach the highest performance of PSCs.

As demonstrated by the present study, SPM techniques as tools to explore the nanoworld have played and continuously play an important role in the research field of PSCs. In particular, operation modes analysing simultaneously the local morphology of the photoactive layer and measuring functional (optical and electrical) properties with nanometre resolution at the same spot contribute in establishing new insights required to commercially produce the high-performance PSCs of the future.

**Acknowledgements.** We would like to thank Xiaoniu Yang, Evgueny Klimov, Denis Ovchinnikov, Wei Zhen Li and Hanfang Zhong for their important assistance in major parts of the work presented. We thank René Janssen, Martijn Wienk, Jeroen van Duren, Sjoerd Veenstra and Marc Koetse for fruitful discussions. Part of the work is embedded in the research program of the Dutch Polymer Institute (DPI projects 326 and 524), and additional financial support is appreciated from the Ministry of Economic Affairs of the Netherlands via the Technologische Samenwerkings project QUANAP (SenterNovem TSGE3108).

## References

1. van Duren JKJ, Loos J, Morrissey F, Leewis CM, Kivits KPH, van IJzendoorn LJ, Rispens MT, Hummelen JC, Janssen RAJ (2002) Adv Funct Mater 12:665
2. Bube RH (1992) Photoelectronic properties of semiconductors. Cambridge University Press Cambridge
3. Pope M, Swenberg CE (1999) Electronic processes in organic crystals and polymers. Oxford University Press, Oxford
4. Tang CW (1998) Appl Phys Lett 48:183
5. Peumans P, Yakimov A, Forrest SR (2003) J Appl Phys 93:3693
6. Smilowitz L, Sariciftci NS, Wu R, Gettinger C, Heeger AJ, Wudl F (1993) Phys Rev B 47:13835
7. Yoshino K, Hong YX, Muro K, Kiyomatsu S, Morita S, Zakhidov AA, Noguchi T, Ohnishi T (1993) Jpn J Appl Phys Part 2 32:L357

8. Halls JJM, Pichler K, Friend RH, Moratti SC, Holmes AB (1996) Appl Phys Lett 68:3120
9. Haugeneder A, Neges M, Kallinger C, Spirkl W, Lemmer U, Feldmann (1999) J Phys Rev B 59:15346
10. Yang X, Loos J (2007) Macromolecules 40:1353
11. Yu G, Heeger AJ (1995) J Appl Phys 78:4510
12. Halls JJM, Walsh CA, Greenham NC, Marseglia EA, Friend RH, Moratti SC, Holmes AB (1995) Nature 376:498
13. Yu G, Gao J, Hummelen JC, Wudl F, Heeger AJ (1995) Science 270:1789
14. Yang X, van Duren JKJ, Janssen RAJ, Michels MAJ, Loos J (2004) Macromolecules 37:2151
15. Schmidt-Mende L, Fechtenkötter A, Müllen K, Moons E, Friend RH, MacKenzie JD (2001) Science 293:1119
16. Yang X, Loos J, Veenstra SC, Verhees WJH, Wienk MM, Kroon JM, Michels MAJ, Janssen RAJ (2005) Nano Lett 5:579
17. Becker H, Spreitzer H, Kreuder W, Kluge E, Schenk H, Parker I, Cao Y (2000) Adv Mater 12:42
18. Hummelen JC, Knight BW, LePeq F, Wudl F, Yao J, Wilkins CL (1995) J Org Chem 60:532
19. van Duren JKJ, Yang X, Loos J, Bulle-Lieuwma CWT, Sieval AB, Hummelen JC, Janssen RAJ (2004) Adv Funct Mater 14:425
20. Veenstra SC, Verhees WJH, Kroon JM, Koetse MM, Sweelssen J, Bastiaansen JJAM, Schoo HFM, Yang X, Alexeev A, Loos J, Schubert US, Wienk MM (2004) Chem Mater 16:2503
21. Koch N, Elschner A, Schwartz J, Kahn A (2003) Appl Phys Lett 82:2281
22. Lin H-N, Lin H-L, Wang S-S, Yu L-S, Perng G-Y, Chen S-A, Chen S-H (2002) Appl Phys Lett 81:2572
23. Wudl F (1992) Acc Chem Res 25:157
24. Shaheen SE, Brabec CJ, Sariciftci NS, Padinger F, Fromherz T, Hummelen JC (2001) Appl Phys Lett 78:841
25. Mozer A, Denk P, Scharber M, Neugebauer H, Sariciftci NS, Wagner P, Lutsen L, Venderzande D (2004) J Phys Chem 108:5235
26. Padinger F, Rittberger RS, Sariciftci NS (2003) Adv Funct Mater 13:85
27. Waldauf C, Schilinsky P, Hauch J, Brabec CJ (2004) Thin Solid Films 503:451
28. Al-Ibrahim M, Ambacher O, Sensfuss S, Gobsch G (2005) Appl Phys Lett 86:201120
29. Reyes-Reyes M, Kim K, Carrolla DL (2005) Appl Phys Lett 87:083506
30. Ma W, Yang C, Gong X, Lee K, Heeger AJ (2005) Adv Funct Mater 15:1617
31. Mihailetchi VD, van Duren JKJ, Blom PWM, Hummelen JC, Janssen RAJ, Kroon JM, Rispens MT, Verhees WJH, Wienk MM (2003) Adv Funct Mater 13:43
32. Rispens MT, Meetsma A, Rittberger R, Brabec CJ, Sariciftci NS, Hummelen JC (2003) Chem Commun 2116
33. Hoppe H, Niggemann M, Winder C, Kraut J, Hiesgen R, Hinsch A, Meissner D, Sariciftci NS (2004) Adv Funct Mater 14:1005
34. Martens T, D'Haen J, Munters T, Beelen Z, Goris L, Manca J, D'Olieslaeger M, Vanderzande D, Schepper LD, Andriessen R (2003) Synth Met 138:243
35. Hoppe H, Drees M, Schwinger W, Schäffler F, Sariciftci NS (2005) Synth Met 152:117
36. Zhong H, Yang X, deWith B, Loos J (2006) Macromolecules 39:218
37. Yang X, van Duren JKJ, Rispens MT, Hummelen JC, Michels MAJ, Loos J (2004) Adv Mater 16:802
38. Prosa TJ, Winokur MJ, Moulton J, Smith P, Heeger AJ (1992) Macromolecules 25:4364
39. Bao Z, Dodabalapur A, Lovinger A (1996) Appl Phys Lett 69:4108
40. Sirringhaus H, Brown PJ, Friend RH, Nielsen MM, Bechgaard K, Langeveld-Voss BMW, Spiering AJH, Janssen RAJ, Meijer EW, Herwig P, de Leeuw DM (1999) Nature 401:685

41. Sirringhaus H, Tessler N, Friend RH (1998) Science 280:1741
42. Camaioni N, Ridolfi G, Casalbore-Miceli G, Possamai G, Maggini M (2002) Adv Mater 14:1735
43. Chirvase D, Parisi J, Hummelen JC, Dyakonov V (2004) Nanotechnology 15:1317
44. Toney MF, Russell TP, Logan JA, Kikuchi H, Sands JM, Kumar SK (1995) Nature 374:709
45. Hayakawa T, Wang J, Xiang M, Li X, Ueda M, Ober CK, Genzer J, Sivaniah E, Kramer EJ, Fisher D A (2000) Macromolecules 33:8012
46. Yang X, Alexeev A, Michels MAJ, Loos J (2005) Macromolecules 38:4289
47. Halls JJM, Arias AC, MacKenzie JD, Wu W, Inbasekaran M, Woo WP, Friend RH (2000) Adv Mater 12:498
48. Breeze AJ, Schlesinger Z, Carter SA, Tillmann H, Hörhold H-H (2004) Sol Energy Mater Sol Cells 83:263
49. Stalmach U, de Boer B, Videlot C, van Hutten PF, Hadziioannou G (2000) J Am Chem Soc 122:5464
50. Zhang F, Jonforsen M, Johansson DM, Andersson MR, Inganäs O (2003) Synth Met 138:555
51. Koetse MM, Sweelssen J, Hoekerd KT, Schoo HFM, Veenstra SC, Kroon JM, Yang X, Loos J (2006) Appl Phys Lett 88:083504
52. Loos J, Yang X, Koetse MM, Sweelssen J, Schoo HFM, Veenstra SC, Grogger W, Kothleitner G, Hofer F (2005) J Appl Polym Sci 97:1001
53. Kawata S, Inouye Y (2002) In: Chalmers J, Griffiths P (eds) Handbook of vibrational spectroscopy, vol 1. Wiley-VCH, Chichester, p 1460
54. McNeill CR, Frohne H, Holdsworth JL, Frust JE, King BV, Dastoor P C (2004) Nano Lett 4:219
55. Klimov E, Li W, Yang X, Hoffmann GG, Loos J (2006) Macromolecules 39:4493
56. Alvarado SF, Rieß W, Seidler PF, Strohriegl P (1997) Phys Rev B 56:1269
57. Rinaldi R, Cingolani R, Jones KM, Baski AA, Morkoc H, Di Carlo A, Widany J, Della Sala F, Lugli P (2001) Phys Rev B 63:075311
58. Kemerink M, Alvarado SF, Müller P, Koenraad PM, Salemink HWM, Wolter JH, Janssen RAJ (2004) Phys Rev B 70:045202
59. Huser T, Yan M (2001) Synth Met 116:333
60. Hoppe H, Glatzel T, Niggemann M, Hinsch A, Lux-Steiner MC, Sariciftci NS (2005) Nano Lett 5:269
61. Nonnenmacher M, O'Boyle MP, Wickramasinghe HK (1991) Appl Phys Lett 58:2921
62. Shafai C, Thomson DJ, Simard-Normandin M, Mattiussi G, Scanlon P (1994) J Appl Phys Lett 64:342
63. De Wolf P, Snauwaert J, Clarysse T, Vandervorst W, Hellemans L (1995) Appl Phys Lett 66:1530
64. Kelley TW, Frisbie CD (2000) J Vac Sci Technol B 18:632
65. Morgado J, Friend RH, Cacialli F (2000) Synt Met 114:189
66. Brabec CJ, Sariciftci NS, Hummelen JC (2001) Adv Funct Mater 11:15
67. Padinger F, Fromherz T, Denk P, Brabec C, Zettner J, Hierl T, Sariciftci N (2001) Synth Met 121:1605
68. Hoppe H, Sariciftci NS (2006) J Mater Chem 16:45
69. Sugimura H, Ishida Y, Hayashi K, Takai O, Nakagiri N (2002) Appl Phys Lett 80:1459
70. Alexeev A, Loos J, Koetse MM (2006) Ultramicroscopy 106:191
71. Heinz WF, Hoh JH (1999) Trends Biotechnol 17:143
72. Eyben P, Xu M, Duhayon N, Clarysse T, Callewaert S, Vandervorst W (2002) J Vac Sci Technol B 20:471
73. Blom PWM, de Jong MJM, Vleggaar JJM (1996) Appl Phys Lett 68:3308
74. Tanase C, Blom PWM, de Leeuw DM (2004) Phys Rev B 70:193202